
# Deciphering SO2 poisoning mechanisms for passive NOx adsorption: A kinetic modeling approach and development of a high-resistance catalyst

Chemical Engineering Journal 487 (2024) 150406

Contents lists available at ScienceDirect

Chemical Engineering Journal

journal homepage: www.elsevier.com/locate/cej

# Deciphering $SO_2$ poisoning mechanisms for passive $NO_x$ adsorption: A kinetic modeling approach and development of a high-resistance catalyst

Dawei Yao [a], Phuoc Hoang Ho [a], Johann C. Wurzenberger [b], Thomas Glatz [b], Wei Di [a], Rojin Feizie Ilmasani [a], Derek Creaser [a], Louise Olsson [a,*]

[a] Chemical Engineering division, Competence Center for Catalysis, Chalmers University of Technology, Göteborg SE-41296, Sweden
[b] AVL List GmbH, Graz, Austria

ARTICLE INFO

*Keywords:*
Passive NOx adsorption (PNA)
Pd/SSZ-13
Sulfur poisoning
Kinetic modelling
Synthesis method

ABSTRACT

Passive NOx adsorption (PNA) is a promising technology aimed at reducing $NO_x$ emissions from vehicles during the cold start phase of the engine. This work investigated the $SO_2$ poisoning mechanism of PNA through a combination of experimental research and kinetic modeling, leading to the development of a novel PNA sample with high resistance to $SO_2$ poisoning. Pd/SSZ-13 samples were synthesized using different drying conditions, revealing that samples dried at room temperature showed lower degradation (10 %) compared to those dried at 80 °C (26 %). Investigation into the degradation revealed that ion-exchanged Pd sites with a hydroxyl group were more resistant to $SO_2$ poisoning than other Pd sites. It is also found that $SO_2$ aids in $NO_x$ storage on Pd sites, enhancing the PNA performance. A kinetic model was developed to describe the $SO_2$ poisoning behavior and its influence on $NO_x$ storage. The model, which was verified under various conditions, effectively simulated the PNA behavior and $SO_2$ poisoning of Pd/SSZ-13.

## 1. Introduction

With the increasing global transportation sector, gasoline and diesel engines still have a great share in the production of new vehicles [1]. During the cold start of the engine, the nitrogen oxides ($NO_x$) are inevitably formed and become a main environmental issue. The cold start phase is characterized by the ignition of the engine and the subsequent thermal elevation of the engine block, tailpipe, and catalysts from their ambient temperature [2]. The efficiency of the exhaust after-treatment system in mitigating emissions experiences a substantial reduction during this phase owing to kinetic constraints. As emission regulations become increasingly stringent, coupled with the reduction in engine exhaust temperatures due to advancements in fuel efficiency, the need to address cold start emissions has been magnified [3].

Over recent years, Passive $NO_x$ Adsorbers (PNAs) have emerged as a significant area of interest due to their potential to address the persistent challenge of $NO_x$ emissions during the cold start phase in automotive exhaust systems [4]. PNAs exhibit a unique functionality due to their capacity to temporarily store $NO_x$ at low temperatures. This capability enables the adsorption of $NO_x$ during the cold start phase. Thereafter, when the temperature is further increased typically above ~ 200 °C the urea can be dosed and the $NH_3$-Selective Catalytic Reduction (SCR) system can operate. Thus, at higher temperature when the NOx are desorbed from the PNA it can be reduced in the following SCR unit and thereby receiving a high NOx conversion both at low and high temperature. To thoroughly appraise the effectiveness and potential applicability of PNAs, several key parameters must be considered, including the $NO_x$ storage at low temperatures, adsorption rate, $NO_x$ desorption temperature, compatibility with real exhaust conditions, resistance to degradation, and cost-efficiency [5].

Like most after-treatment catalysts, PNAs often experience significant thermal aging and poisoning. During PNA performance evaluations, this degradation is typically reflected in a decrease in low-temperature $NO_x$ storage capacity and a shift in the desorption temperature into a non-optimal range. Therefore, understanding the material transformations that occur during aging and poisoning is essential for enhancing catalyst stability. There is growing interest in Pd-impregnated zeolites for PNA applications. Specifically, palladium loaded on small-pore zeolites, such as SSZ-13, have shown potential due to their comparatively appropriate $NO_x$ desorption temperature window [6,7] and excellent tolerance to $H_2O$ [5,8]. However, the stability of Pd/SSZ-13 in the PNA process can be compromised by the presence of CO,

* Corresponding author.
*E-mail address:* louise.olsson@chalmers.se (L. Olsson).

https://doi.org/10.1016/j.cej.2024.150406
Received 4 December 2023; Received in revised form 5 March 2024; Accepted 12 March 2024
Available online 13 March 2024

phosphorus, and sulfur. Previous reports indicate that high CO concentration can trigger Ostwald ripening of ion-exchanged Pd sites and particle migration of external PdO sites, consequently leading to the degradation of PNA performance [9,10]. Phosphorous is also recognized to cause both physical and chemical deactivation of Pd/SSZ-13, including the physical blockage of active Pd sites by $P_2O_5$ and dealumination of the zeolite framework caused by the formation of $AlPO_4$ [11–13]. A recent patent from Johnson Matthey showed approximately 25 % degradation of PNA performance following sulfur poisoning [14].

However, among the current research, there is no conclusion on the mechanism of sulfur poisoning, or how to design a PNA sample that maintains stability in the presence of sulfur during the PNA process. In this work we, for the first time in literature, present a kinetic model that can describe the sulfur poisoning of Pd/SSZ-13, used as a PNA. In addition, we have developed the synthesis method for Pd/SSZ-13 and we have successfully enhanced the sulfur resistance of the PNA. In more detail, we synthesized a typical Pd/SSZ-13 using an impregnation method and then modified the drying process after impregnation to achieve different surface Pd site distributions. By varying the quantity of different surface Pd active sites, we were able to examine the stability of these Pd sites during sulfur poisoning in a multicycle PNA evaluation. The PNA experiments clearly showed that the modified synthesis method resulted in a PNA with higher sulfur resistance. The PNA samples were characterized before and after the multicycle test, and it was demonstrated that the different Pd active sites changed after sulfur poisoning. After collecting experimental data, we were able to develop a kinetic model to describe both the PNA performance and sulfur poisoning behavior, as well as the enhancement of $NO_x$ storage by sulfur during the multicycle PNA test. This kinetic model can also simulate PNA performance under varying sulfur concentrations and adsorption temperatures.

## 2. Experiment

### 2.1. Synthesis of passive $NO_x$ adsorber

#### 2.1.1. Synthesis of SSZ-13

SSZ-13 zeolites with a SAR of 12 were synthesized using a hydrothermal method reported from our previous works [12,15–17]. In summary, a gel was formed by vigorously stirring a mixture of 1.6 g NaOH, 35.16 g TMAda-OH, 2.76 g $Al(OH)_3$, and 24 g $SiO_2$ in 132 mL of deionized water. The resulting mixture was then transferred into an autoclave and heated at 160 °C for 96 h with rotational stirring. After being cooled to ambient temperature, the mixture underwent a centrifugation washing process using 900 mL of water that had been deionized. The resulting product was then dried at 80 °C for 6 h and subsequently calcined at 600 °C for 8 h. $NH_4$-SSZ-13 was synthesized through an ion-exchange procedure. Specifically, a mixture was prepared by combining 15 g of Na-SSZ-13 with 300 mL of 1 M $NH_4NO_3$ solution, which was then heated up to a temperature of 80 °C. The resulting mixture was washed with 800 mL of deionized water. To ensure the complete removal of Na ions, the procedure of ion-exchange was performed two additional times. The resulting sample was subsequently dried at 80 °C for six hours.

The Pd/SSZ-13 samples were prepared using incipient wetness impregnation, where a $Pd(NO_3)_2$ solution was used to load 1 wt% Pd onto $NH_4$-SSZ-13. The resulting sample was subjected to different drying procedures (all drying was conducted in air). In one approach, the sample was dried at room temperature for 48 h. After drying, the sample underwent a calcination process at a temperature of 500 °C sustained for a duration of 5 h, and referred to as 'Roomdry'. In contrast, a different sample was subjected to an overnight drying process at 80 °C and a 5-hour calcination at 500 °C, a standard procedure for loading Pd on SSZ-13 [6,12,16]. This sample was subsequently termed as '80dry'.

#### 2.1.2. Monolith preparation

The cordierite monoliths were structured in a honeycomb shape with a cell density of 400 cpsi. The monoliths were then sliced into small cylinders measuring 2 cm in length and 2.1 cm in diameter. To clean the channel surfaces, the monoliths were calcined at 550 °C for 2 h. After that, a mixture of 95 wt% Pd/SSZ-13 powder and 5 wt% Boehmite (Dispersal P2) was mixed in an ethanol/$H_2O$ (1:1) solution. The mixture was then introduced into the channels of the monoliths and dried at 80 °C. This procedure was repeated several times until the desired weight of the washcoat was reached (700 ± 7 mg). Finally, the loaded monoliths were calcined at 500 °C for 5 h.

### 2.2. Evaluation of the passive $NO_x$ adsorber

#### 2.2.1. Multicycling experiments

As we described in our previous studies [15,18–20], the PNA evaluation system consists of multiple mass flow controllers, a system dedicated to $H_2O$ evaporation, a reactor tube equipped with a pair of thermocouples, along with a Fourier Transform Infrared (FTIR) spectrometer, specifically the MKS Multigas 2030 variant. The cordierite monolith was positioned within the reactor tube, and two thermocouples were positioned upstream of the monolith and inside the monolith channel, respectively.

#### 2.2.2. Degreening process

To enhance the Pd sites generated during the ion-exchange phase and to ensure the stability of the PNA sample, a degreening process was carried out on all the samples prior to material characterization and PNA evaluation [21]. The monolith, once positioned in the reactor, was subjected to a treatment at 750 °C under a total flow rate of 900 mL/min with 400 ppm $NO_x$, 5 % $H_2O$, and 8 % $O_2$. After the treatment, the monolith was purged with Ar at 750 °C to eliminate any adsorbed species and then cooled down to either 80 °C for the subsequent evaluation or to room temperature for further characterizations. Notably, to confirm the absence of any pre-adsorbed species on the monolith, two test cycles under identical conditions were performed prior to $SO_2$ poisoning. Consistent $NO_x$ storage behavior across these cycles indicates the successful removal of pre-adsorbed species following the degreening process.

#### 2.2.3. Evaluation process

After undergoing the degreening process, the PNA samples were evaluated over 12 cycles to assess their performance with and without $SO_2$. Cycles 3–7 included the addition of 26–104 ppm $SO_2$ at 390 ppm $NO_x$, 4.6 % $H_2O$, and 6.9 % $O_2$, while cycles 1, 2, and 8 were conducted without $SO_2$. The evaluation process is shown in Fig. 1. Each evaluation cycle consisted of three stages that simulated the cold start period of an engine.

The first stage involved $NO_x$ adsorption at a low temperature of 80 °C to 150 °C, with the gas mixture containing 200 ppm $NO_x$, 26–104 ppm $SO_2$ (added in cycles 3–7), 5 % $H_2O$, 8 % $O_2$, and the balance in Ar. The $NO/NO_x$ ratio was 0.982. This stage was maintained for 45 min.

In the second stage, temperature-programmed desorption (TPD) was conducted. While keeping the gas conditions identical, the temperature was gradually increased to 550 °C at a rate of 10 °C/min and then held for 15 min.

In the third stage, the regeneration process was conducted. For cycles 1, 2, and 8–12, $NO_x$ was first stopped. Following that, the system's temperature was kept at 550 °C for 5 min before being cooled down to the adsorption temperature for the next cycle. For cycles with $SO_2$, both $NO_x$ and $SO_2$ were stopped, lowered to the adsorption temperature for the following cycle, without holding the temperature at 550 °C.

The total $NO_x$ storage capacity is determined from the desorption branch of the $NO_x$ profile, utilizing the equation below:

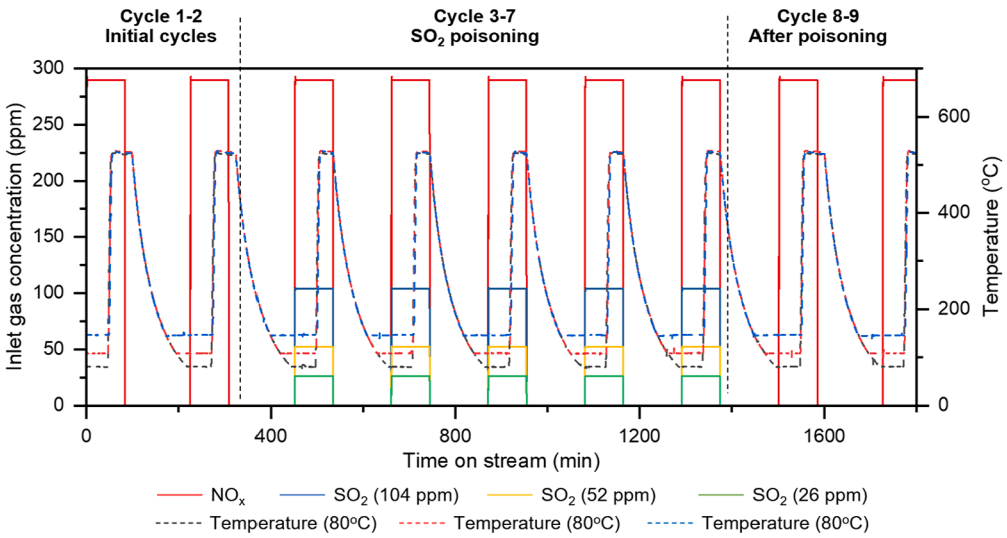


**Fig. 1.** Multicycle evaluation process was conducted on a PNA sample to assess its performance under different concentrations of $SO_2$ and at varying adsorption temperatures. The other reaction conditions included $NO_2/NO_x$ at 1.8 %, 4.6 % $H_2O$, and 6.9 % $O_2$ in Ar, with a flow rate of 905 mL/min.

$$n = \int_{t=45min}^{t=60min} Q \times [c_{out}(t) - c_{in}(t)]dt \quad (1)$$

where $n$ represents the total $NO_x$ stored, $Q$ is the total flow rate, $t$ is the reaction time, $c_{out}$ and $c_{in}$ are the $NO_x$ concentration at the outlet and inlet, respectively.

### 2.3. Characterization methods

An FEI Tecnai microscope was utilized for conducting Transmission Electron Microscopy (TEM), operated at a voltage of 200 kV. To set up the TEM sample, the powder was dispersed in ethanol and placed on a copper grid underpinned by a carbon film. To gather statistical data pertaining to the diameters and the average diameter of nearly 100 Pd particles in each specimen, the TEM images were analyzed.

Measurements using X-ray diffraction (XRD) were performed employing a Bruker D8 Discover apparatus, set at a voltage of 40 kV and a current of 40 mA. The radiation source was Cu Kα radiation (λ = 1.5418 Å), which was filtered at ambient temperature. The resulting XRD pattern was achieved through a scanning range of 10° to 60°, at a rate of 1° per minute.

To analyze standard powder samples, a Scanning Electron Microscope (SEM, JEOL 7800F Prime) was utilized. Samples were gold-sputter-coated for conductivity and examined under a high-resolution SEM at 20 kV. Imaging focused on surface morphology and particle size, with magnifications from 1000x to 25000x. Multiple areas were scrutinized, and representative micrographs were captured.

The nitrogen physisorption test for Pd/SSZ-13 was conducted using a Micromeritics ASAP 2020. The experiment aimed to determine the specific surface area of the palladium-loaded SSZ-13 zeolite. Prior to measurement, the sample was degassed under vacuum at 150 °C to remove moisture and other adsorbed gases. Nitrogen gas was then adsorbed onto the sample at liquid nitrogen temperature. The amount of gas adsorbed at various pressures was measured to construct an adsorption isotherm. The Brunauer-Emmett-Teller (BET) theory was applied to the isotherm to calculate the specific surface area of Pd/SSZ-13.

Diffuse reflectance infrared Fourier transform spectroscopy (DRIFTS) was performed using a Bruker Vertex 70 spectrometer, with an in-situ diffuse chamber, an MCT detector and CaF windows. The gas mixture was controlled by mass flow controllers and an $H_2O$ evaporator. The Pd/SSZ-13 samples, either degreened or tested, were scratched from the monolith wall and 20 mg of the powder was placed in the chamber. For in-situ DRIFT of CO adsorption, the samples were then pretreated at 200 °C under pure Ar and cooled down to 30 °C. After cooling to 30 °C, the background was measured. CO adsorption was measured by scanning at 30 °C with a resolution of 4 $cm^{-1}$. During 20 min, 4000 ppm CO in Ar was added, followed by pure Ar for 5 min to flush out the gas phase CO. For the operando DRIFT of $NO_x$ and $SO_2$ co-adsorption, $NO_x$ adsorption was first conducted by exposing the samples to 390 ppm $NO_x$ and 6.9 % $O_2$ in Ar for 30 min at 80 °C, with a subsequent addition of 104 ppm $SO_2$ in Ar for another 30 min. After exposure, the system was flushed with pure Ar for 5 min to remove residual gases.

The process of CO chemisorption was carried out utilizing an ASAP 2020 Chemi Plus instrument from the Micromeritics Instruments Corporation, which comes equipped with an additional chemisorption device. The powder was positioned in a tube and sealed within the device, which was followed by a pretreatment at 200 °C Celsius under a vacuum to eliminate any possible contaminants. Post-pretreatment, the tube's temperature was reduced to 35 °C, and CO was introduced ranging from 0.13 to 0.80 bar to capture the initial adsorption isotherm. The isotherm was then repeated after conducting an evacuation process to remove the CO from physisorption. The difference between the two isotherms provided the amount of chemisorbed CO.

### 2.4. Experimental results

#### 2.4.1. Physicochemical properties of Pd/SSZ-13 samples

Scanning Electron Microscopy (SEM) images of SSZ-13 samples, prepared under room-dried and 80 °C-dried conditions, were captured at magnifications of x5000, x10000, and x20000, as shown in Fig. 2. The images consistently demonstrated similar morphologies for both drying conditions, highlighting the crystalline structure characteristic of the SSZ-13 zeolite. The SEM analysis provided a clear depiction of the zeolite's uniform and well-defined crystalline features.

Table 1 outlines the physicochemical properties of Pd/SSZ-13 samples dried at room temperature (Roomdry) and 80 °C (80dry). The surface area of the Roomdry sample is 764.2 m2/g, surpassing the 80dry's 681.4 m2/g, which suggests that higher drying temperatures may decrease surface area. However, pore volumes and sizes are closely matched, with the Roomdry at 0.068 $cm^3$/g and 41.8 Å, and the 80dry at 0.060 $cm^3$/g and 41.4 Å, indicating that drying conditions do not significantly alter the pore structure, maintaining the porous architecture essential for their performance in $NO_x$ adsorption and release processes.

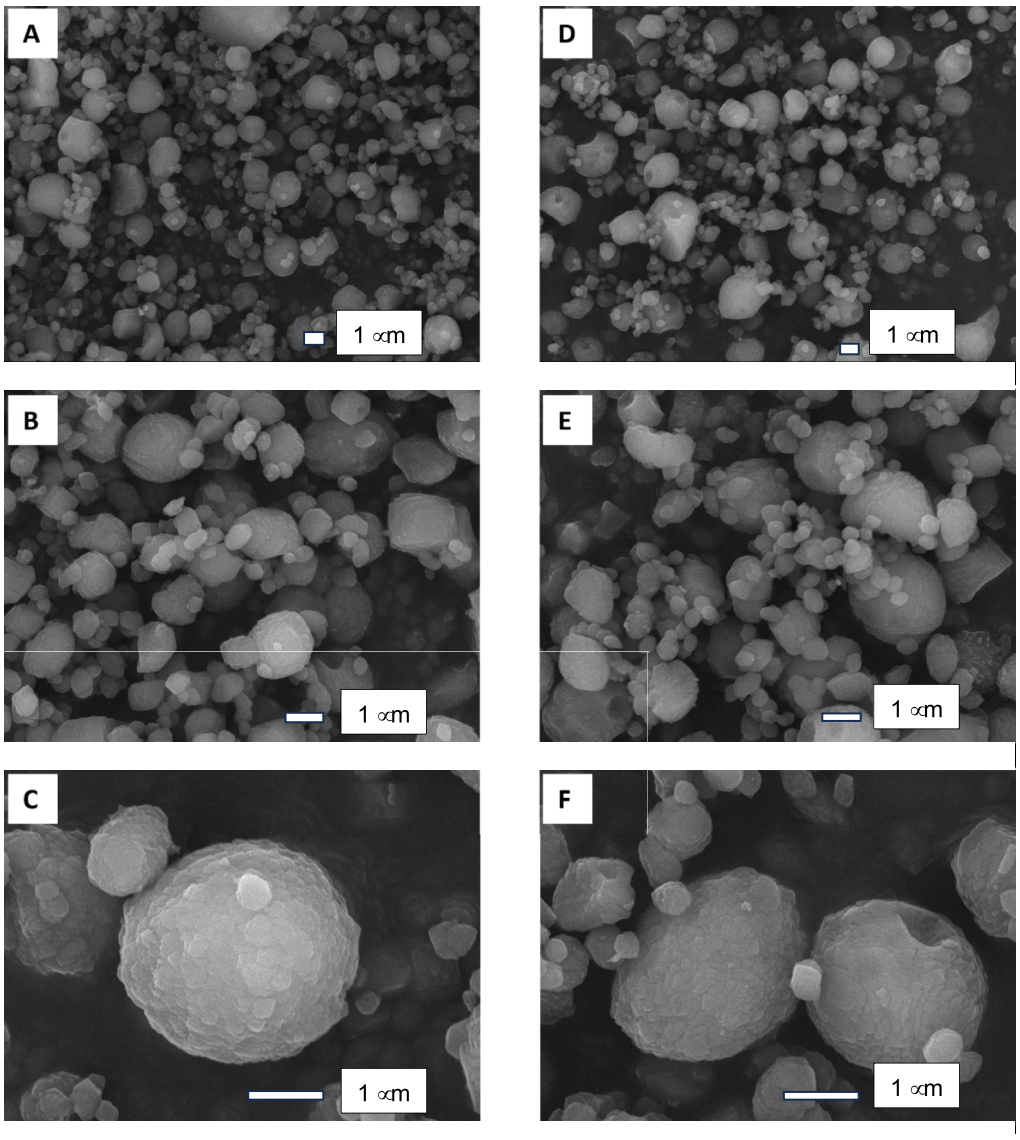


**Fig. 2.** SEM images of Pd/SSZ-13 sample. A-C: Images for Roomdry. D-F: Images for 80dry.

**Table 1**
Physicochemical properties of Pd/SSZ-13 samples.

| Sample | Surface area (m2/g)[a] | Pore volume (cm3/g)[b] | Pore size (Å)[b] |
|---|---|---|---|
| 1 %Pd/SSZ-13 Roomdry | 764.2 | 0.068 | 41.8 |
| 1Pd/SSZ-13 80dry | 681.4 | 0.060 | 41.4 |

[a] calculated by Brunauer-Emmett-Teller (BET) method.
[b] calculated by Barrett-Joyner-Halenda method (BJH) method based on desorption branch.

### 2.4.2. $No_x$ adsorption and release in multicycle PNA Test, including $SO_2$ poisoning

The $NO_x$ storage and release performance, as well as $SO_2$ poisoning behavior, were examined over the Pd/SSZ-13 samples that were either dried after palladium impregnation at room temperature ("Roomdry") or at 80 °C ("80dry"). These two samples were evaluated over 12 PNA cycles, where cycles 3–7 included an addition of 104 ppm $SO_2$, while the other cycles were conducted without $SO_2$. The operating temperature on the adsorption branch of each cycle was set to 80 °C. To facilitate the comparison between different cycles, the time points of $NO_x$ injection in every cycle were considered as the beginning of each cycle (Time of stream = 0). We selected Cycle 2 (the last cycle before $SO_2$ addition), Cycle 3 (the first cycle with $SO_2$ addition), Cycle 7 (the last cycle with $SO_2$ addition), and Cycle 8 (the first cycle after $SO_2$ shut off) to represent the $NO_x$ storage and release performance, and $SO_2$ poisoning behavior in this multicycle PNA test. Their respective NO and $NO_2$ profiles are displayed in Fig. 3. The full-cycle performance is shown in Fig. S1, Supplementary Information (SI). There was no degradation of PNA performance prior to the addition of $SO_2$, as evidenced by the lack of change between cycles 1 and 2 (Fig. S1A, D). Similarly, no degradation of PNA performance was observed between cycles 9 and 12 (Fig. S1C, F), suggesting sample stability after poisoning. Therefore, we primarily focused on cycles 2–9 in subsequent experimental and modeling work.

In Fig. 3, we observe two NO release peaks at 290 °C and 460 °C, and NO oxidation to $NO_2$ peaks at 150–180 °C for both PNA samples. This suggests the presence of at least two Pd sites for NO storage and another Pd site for $NO_2$ formation. Notably, the peak around 2750 s marks the start of NO release at 290 °C. Based on previous kinetic modeling work on PNA [16,17,22,23], the NO oxidation to $NO_2$ peaks at 150–180 °C can be attributed to the reduction of ion-exchanged Pd sites with a hydroxyl group ($Z^-[Pd(II)OH]^+$) to lower valence ion-exchanged Pd sites ($Z^-Pd(I)$), as this reaction has relatively low activation energy compared

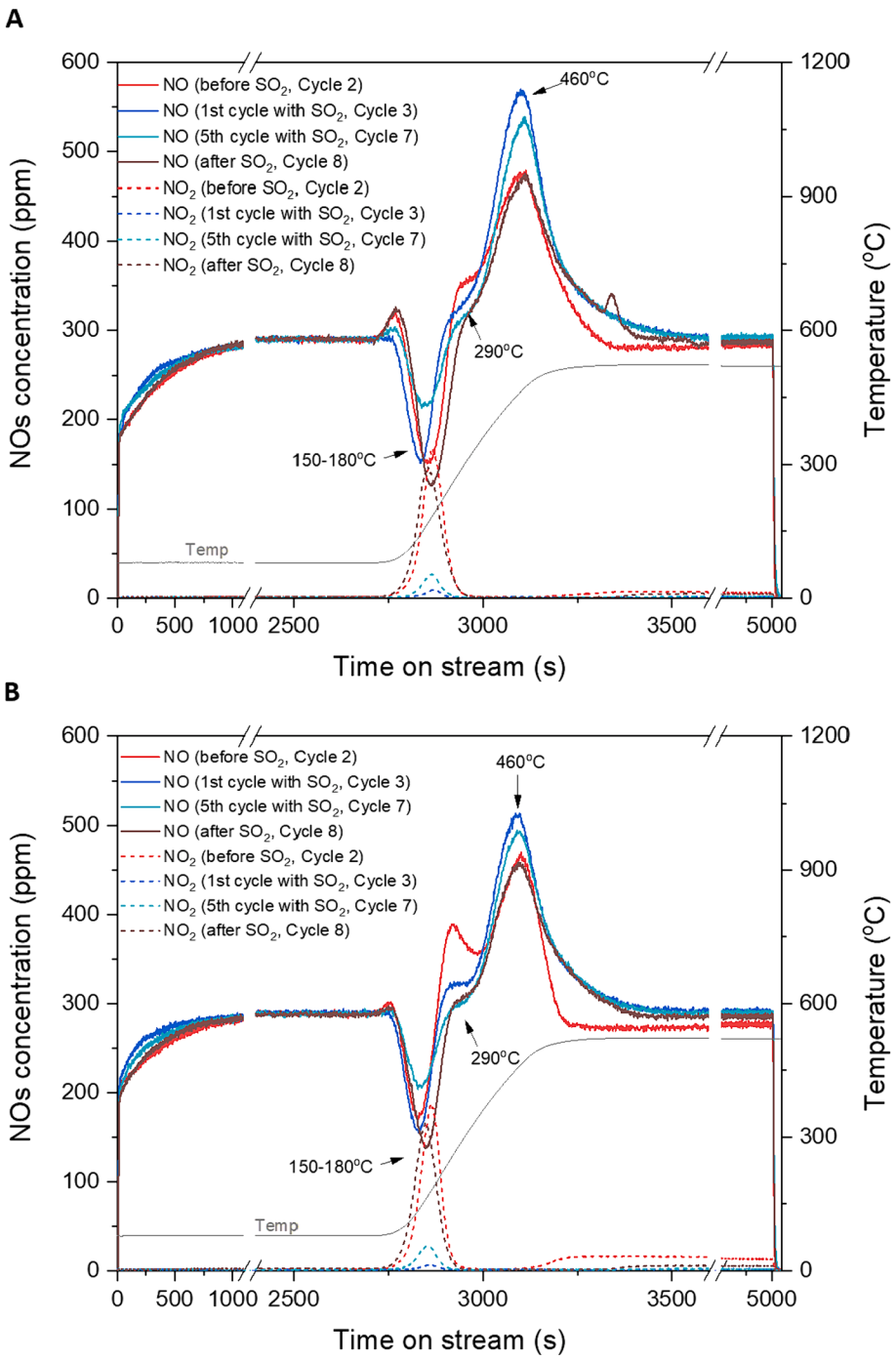


**Fig. 3.** PNA and $SO_2$ poisoning performance of Roomdry (A) and 80dry (B) in selected cycles. Reaction conditions: 290 ppm $NO_x$, $NO_2/NO_x$ = 1.8 %, 104 ppm $SO_2$ (only in Cycle 3–7), 4.6 % $H_2O$, 6.9 % $O_2$ in Ar with the flow rate of 905 mL/min. Adsorption temperature: 80 °C. 'Roomdry' and '80dry' denote the Pd/SSZ-13 samples which were dried at room temperature or 80 °C after Pd impregnation.

to the reduction of other Pd site reactions [24]. The formation and decomposition of Pd nitrates on PdO also contribute to these NO oxidation to $NO_2$ peaks [25].

With the presence of $SO_2$ from cycles 3 to 7, it is clear that the $NO_2$ generation at 150–180 °C was markedly suppressed, while the NO consumption peak at the same temperature persisted. These results suggest that $SO_2$ can inhibit the reduction of $Z^-[Pd(II)OH]^+$ or directly cover the surface of $Z^-[Pd(II)OH]^+$. Simultaneously, $SO_2$ may also hinder the formation of Pd nitrates but provide another site for NO adsorption at the same temperature.

The NO desorption peaks at 290 °C and 460 °C can be attributed to the release of NO species from $Z^-Pd(II)Z^-$ and $Z^-Pd(I)$, respectively, in accordance with the adsorption energies of NO on these different Pd sites [16,17,24]. The $Z^-Pd(II)Z^-$–NO peak in the 80dry sample is much larger than that in the Roomdry sample, indicating that drying at 80 °C generates more ion-exchanged Pd sites without a hydroxyl group, while room-drying tends to produce more hydroxyl groups on ion-exchanged Pd sites.

Upon the addition of $SO_2$, both $Z^-Pd(II)Z^-$–NO peaks on Roomdry and 80dry samples decreased significantly, with a more pronounced decrease in the 80dry sample due to its larger initial quantity. This suggests that $Z^-Pd(II)Z^-$ sites are susceptible to $SO_2$ poisoning, either by

being covered by $SO_2$ species or converted to another inactive Pd species. In contrast, the $Z^-[Pd(II)OH]^+$–NO (released at 460 °C) is considerably more stable than $Z^-Pd(II)Z^-$–NO, as evidenced by its peak intensity remaining unchanged before and after $SO_2$ poisoning (in cycle 2 and cycle 8). During cycles 3 to 7, the existing $SO_2$ even appeared to aid NO adsorption on $Z^-[Pd(II)OH]^+$–NO as the related peak increased. This finding also suggests that the remaining NO adsorption peak at 150–180 °C after adding $SO_2$ may be attributed to the increase of the NO desorption peak at 460 °C, since the mass of $NO_x$ adsorption and desorption should be balanced. Notably, the slight peak increase at approximately 3300 s in cycle 8 results from minor disturbance due to unstable $H_2O$ injection.

Fig. 4A illustrates the calculated $NO_x$ storage amount and the $NO_x$/Pd ratio for each cycle of the Roomdry sample under varying $SO_2$ concentrations. Interestingly, upon addition of 104 ppm $SO_2$, the $NO_x$ adsorption amount rose from $3.0 \times 10^{-4}$ mol per monolith to $4.2 \times 10^{-4}$ mol per monolith, then gradually declined in the subsequent cycles. With the decreasing concentration of $SO_2$, the adsorption amount of $NO_x$ also proportionally decreased. Conversely, changes in $SO_2$ concentration did not have a pronounced effect on the degradation in the multicycle test, especially in cycle 7 when the $SO_2$ inlet was shut off.

These results suggest that $SO_2$ can both enhance $NO_x$ adsorption and deactivate the PNA. For the enhancement aspect, $SO_2$ seems to offer additional adsorption sites for $NO_x$ or allow co-adsorption of $NO_x$ on the same sites, as $NO_x$ demonstrated predominantly singular adsorption on Pd sites in the presence of $H_2O$ prior to $SO_2$ addition [6,16]. The results indicate that the $SO_2$-induced poisoning, after $SO_2$ is removed, is likely due to the blockage of Pd active sites by $SO_2$, since an increase in $SO_2$ concentration only slightly influences the poisoning behavior.

Fig. 4B presents the calculated $NO_x$ desorption amounts and the $NO_x$/Pd ratios for the Roomdry and 80dry samples. In the first two cycles without $SO_2$, the $NO_x$ storage amount is similar for both Roomdry and 80dry, suggesting comparable amounts of exposed Pd sites in both samples. However, as seen from the NO & $NO_2$ profiles in cycle 2 in Fig. 5A, 80dry contains more $Z^-Pd(II)Z^-$ sites capable of releasing NO at 290 °C, while Roomdry has more $Z^-[Pd(II)OH]^+/Z^-Pd(I)$ sites that can release NO at 460 °C. Upon the addition of $SO_2$ from cycle 3, the $NO_x$ storage in 80dry does not increase as significantly as in Roomdry. We suggest that this is due to the lower quantity of $Z^-[Pd(II)OH]^+$ sites in 80dry, which are the adsorption sites that can be strongly enhanced by $SO_2$. The two samples, Roomdry and 80dry, are compared in Fig. 5, for different cycles. As depicted in Fig. 4B and 4C, the NO release peak from $Z^-[Pd(II)OH]^+/Z^-Pd(I)$ (460 °C) in Roomdry is much higher than that in 80dry during sulfur exposure. Following the shutting of $SO_2$ inlet from cycle 8, degradation in 80dry (26 %) is substantially more severe than in Roomdry (10 %) (Fig. 4B), because 80dry contains more $Z^-Pd(II)Z^-$ sites that are vulnerable to $SO_2$. Moreover, the NO desorption peak area in Roomdry is higher than that in 80dry, as Roomdry contains more $Z^-[Pd(II)OH]^+/Z^-Pd(I)$ sites (Fig. 5D).

### 2.4.3. Characterization of Pd sites during $SO_2$ poisoning

To further validate the $SO_2$ poisoning mechanism inferred from the PNA evaluation results, in situ DRIFT of CO adsorption was conducted to determine the distribution of exposed Pd sites in Roomdry and 80dry samples before and after $SO_2$ poisoning, as depicted in Fig. 6A. CO is well-established as a probe molecule stems from its specific binding characteristics, which allow for the precise identification of various Pd active sites on the zeolites. These sites are pivotal in the adsorption process, influencing the catalyst's performance regarding NO. By examining how CO interacts with Pd sites, we can infer the dispersion, oxidation state, and coordination environment of Pd, which are critical factors affecting the adsorption and catalytic behavior towards NO [26,27]. The Pd/SSZ-13 sample was first exposed to 4000 ppm CO/Ar for 20 min at 30 °C, then purged with pure Ar for 5 min to collect the spectra. Peaks at 2211 $cm^{-1}$ and 2190 $cm^{-1}$ was assigned to CO adsorbed on $Z^-Pd(II)Z^-$ sites [28,29], while the peak at 2111 $cm^{-1}$ was attributed to linear adsorption on $Pd/PdO_x$ clusters [13,30]. The peak at 1895 $cm^{-1}$ is attributed to bridged carbonyls of $Pd^0$ and multi-bridged carbonyls on small Pd clusters [31,32]. Peaks at 2127 $cm^{-1}$ and 2146 $cm^{-1}$ are assigned to CO adsorption on ion $Z^-[Pd(II)OH]^+$ complexes [28,32,33], and the peak at 2164 $cm^{-1}$ can be assigned to CO adsorption on the surface of $Z^-[Pd(II)OH]^+$ [13,34,35]. The relative intensity proportion of the CO adsorption peaks, which correspond to different Pd sites, are calculated and listed in Table 2. Compared to the Roomdry sample, more $Z^-Pd(II)Z^-$ sites exist in the 80dry sample; however, they are vulnerable to $SO_2$ poisoning, as evidenced by the decrease in CO-$Z^-Pd(II)Z^-$ peaks at 2211 $cm^{-1}$ and 2190 $cm^{-1}$ after poisoning. Following $SO_2$ poisoning, the relative intensity of linear CO-$Pd^0/PdO_x$ (2211 $cm^{-1}$) decreased in both Roomdry and 80dry, suggesting a reduction in the surface area of $Pd/PdO_x$ after poisoning. This could indicate that $Pd/PdO_x$ sites may be covered by $SO_2$ or that $SO_2$ induced the agglomeration of $Pd/PdO_x$ into larger nanoparticles. The CO-$Z^-[Pd(II)OH]^+$ peaks (2127 and 2146 $cm^{-1}$) are dominant both before and after $SO_2$ poisoning for both Roomdry and 80dry samples, suggesting that the $Z^-[Pd(II)OH]^+$ sites are more stable than other Pd sites. The peak proportion analysis reveals that $Z^-[Pd(II)OH]^+$ is the predominant site across all samples. However, the Roomdry sample contains more stable $Z^-[Pd(II)OH]^+$ sites compared to the 80dry sample. Conversely, the 80dry sample has a higher quantity of $Z^-Pd(II)Z^-$ sites than those found on Roomdry. These observations align with the findings from the PNA evaluation.

To explore the reaction mechanism spectrographically, operando DRIFT spectroscopy of NO and $SO_2$ co-adsorption was performed, as depicted in Fig. 6B. The adsorption process was carried out at 80 °C, using gas concentrations of 390 ppm $NO_x$, 6.9 % $O_2$, and 104 ppm $SO_2$, which align with the conditions used in the PNA tests. It is important to

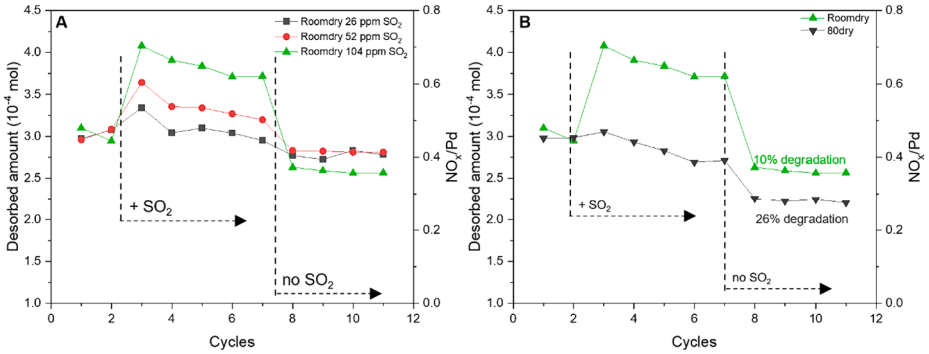


**Fig. 4.** Stored amount of $NO_x$ per monolith (700 mg washcoat) and $NO_x$/Pd in each cycle of PNA test with $SO_2$ poisoning. A: Roomdry sample tested under different $SO_2$ concentrations. B: Roomdry and 80dry sample tested under 104 ppm $SO_2$. 'Roomdry' and '80dry' denote the Pd/SSZ-13 samples which were dried at room temperature or 80 °C after Pd impregnation.

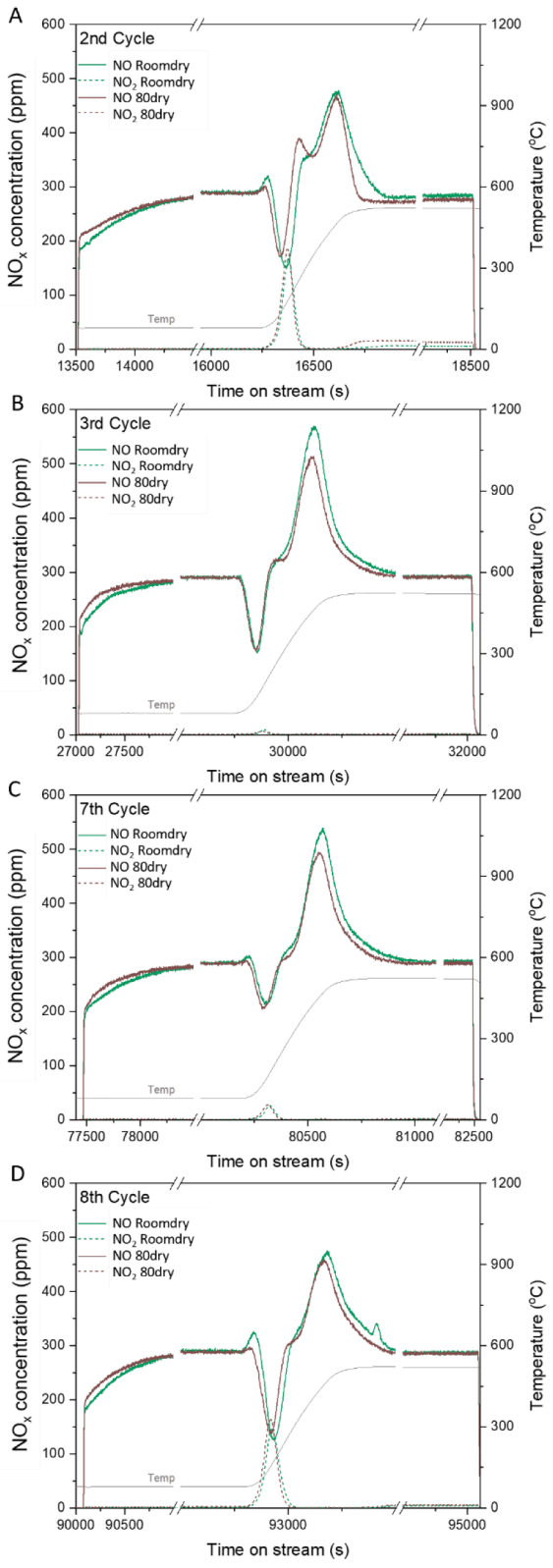


**Fig. 5.** PNA performance of Roomdry and 80dry in Cycle 2 (last cycle without $SO_2$), Cycle 3 (first cycle with $SO_2$), Cycle 7 (last cycle with $SO_2$) and Cycle 8 (first cycle shut $SO_2$). Reaction conditions: 290 ppm $NO_x$, $NO_2/NO_x$ = 1.8 %, 104 ppm $SO_2$ (only in Cycle 3–7), 4.6 % $H_2O$, 6.9 % $O_2$ in Ar with the flow rate of 905 mL/min. Adsorption temperature: 80 °C. 'Roomdry' and '80dry' denote the Pd/SSZ-13 samples which were dried at room temperature or 80 °C after Pd impregnation.

note that $H_2O$ was omitted from the system to prevent the formation of sulfuric acid, which could potentially damage the DRIFT chamber. Analysis of Fig. 6B reveals the presence of peaks at 1360 $cm^{-1}$, 1376 $cm^{-1}$, and 1202 $cm^{-1}$, indicative of bulk sulfate species on aluminum sites [36,37], while the peak at 1256 $cm^{-1}$ is associated with $PdSO_4$ species [36,38,39]. Additionally, the peaks at 1277 $cm^{-1}$ and possibly 1292 $cm^{-1}$ suggest the chemisorption of $SO_2$ on Pd sites [36,37], implying that $SO_2$ chemisorption occurs on ion-exchanged Pd sites. The peak at 1303 $cm^{-1}$ is attributed to physisorbed $SO_2$ [36,37,40]. In conclusion, the DRIFT study indicates two primary forms of $SO_2$ adsorption on the Pd-SSZ-13 samples: chemisorbed $SO_2$ on ion-exchanged Pd sites and $PdSO_4$, both of which are crucial in understanding the $SO_2$ poisoning behavior towards the PNA sample.

XRD was performed on the Pd/SSZ-13 samples to assess the condition of both the SSZ-13 support and Pd sites, as illustrated in Fig. 7. Both the Roomdry and 80dry samples clearly contain well-crystallized SSZ-13. In addition, the diffraction peaks of SSZ-13 can be discerned from the XRD patterns post-PNA test, implying that the $SO_2$ contamination did not notably affect the SSZ-13 structure. The diffraction peak seen at $2\theta = 33.8°$ is a characteristic peak of the PdO(1 0 1) phase. To amplify the differentiation between the peaks in various samples, the XRD patterns within this area are magnified, as demonstrated in the right panel of Fig. 7. The PdO(1 0 1) diffraction peaks are observed at $2\theta = 33.8°$ for fresh Roomdry and 80dry completely overlap each other and in addition, the peaks are broad suggesting that the Pd sites are well dispersed. After the PNA experiments, both the PdO(1 0 1) peaks for Roomdry and 80dry increased, indicating that $SO_2$ may induce agglomeration of Pd/PdOx sites during the PNA process. These results are consistent with the in-situ DRIFT of CO adsorption (Fig. 6A). In addition, the results are supported by TEM (Fig. S2), where the particle size increased from 3.0 nm for degreened Roomdry sample, to 7.7 nm after poisoning with 26 ppm $SO_2$ to 6.7 nm after exposure to 54 ppm $SO_2$.

## 3. Kinetic modelling

The kinetic model used in this work was built upon our previous PNA model that described the PNA performance [17]. We utilized AVL BOOST™, embedded with an aftertreatment module, along with the AVL User Coding Interface for constructing the simulations. The parameters relating to mass transfer and heat transfer were established according to the property database in AVL CRUISE™ M. Further information on the equations and assumptions can be found in our previous works on PNA modeling [15–17].

### 3.1. Reactor model

The design of our reactor model incorporates three critical components: the inlet boundary, the monolith, and the outlet boundary. A single channel model is applied, which is very common for kinetic models of monoliths [16,41–45]. Across the system, we have set 20 grid points: 18 of these are arranged along the axial path within the monolith channels, and the remaining two are designated for the inlet and outlet boundaries. The model consists of both the internal mass transfer within the washcoat as well as the external mass transfer in the gas phase. The film model [46] serves as the basis for our description of external mass transfer. In terms of internal mass transfer, we have employed a pore diffusion model with a constant effective diffusivity, in line with the research advocated by Chatterjee et al [47] and consistently applied in our earlier studies [16,41–45]. Given the low concentration of $NO_x$, the reaction heat associated with adsorption/desorption could be neglected. This simplifying assumption aligns with practices commonly seen in a multitude of kinetic modeling studies [41,42,44,48,49].

### 3.2. Kinetic model

The reaction rate constants are defined by the Arrhenius equation as

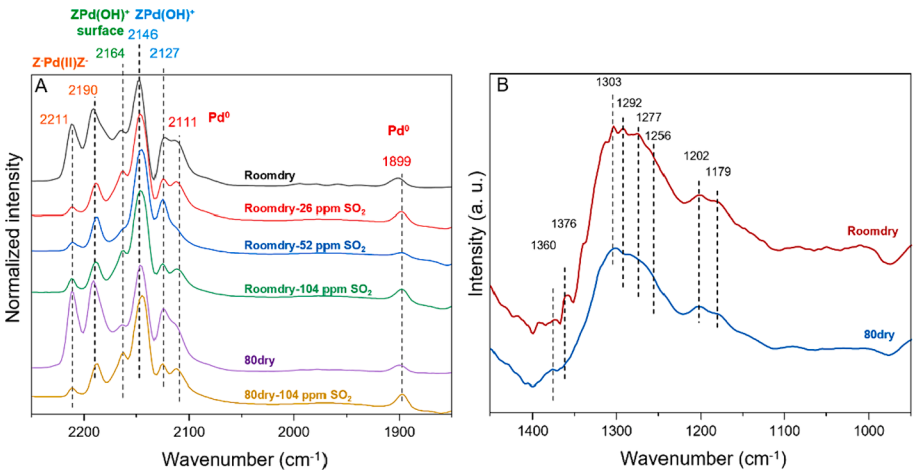


**Fig. 6.** A: in situ DRIFT of CO adsorption on PNA samples prior to and post $SO_2$ contamination. Test condition: 80 °C, 4000 ppm CO, balanced in Ar. B. operando DRIFT of NO and $SO_2$ adsorption on PNA samples. Test conditions: 80 °C, 390 ppm $NO_x$, 6.9 % $O_2$ and 104 ppm $SO_2$, balanced in Ar.

**Table 2**
Peak intensity proportion of all of the ion-exchanged Pd sites ($Z^-Pd(II)Z^-$/$Z^-[Pd(II)OH]^+$) and $Pd/PdO_x$ calculated from in situ DRIFT of CO adsorption as shown in Fig. 6. 'Roomdry' and '80dry' denote the Pd/SSZ-13 samples which were dried at room temperature or 80 °C after Pd impregnation.

| | $Z^-Pd(II)Z^{-a}$ | $Z^-[Pd(II)OH]^+$ | $Pd/PdO_x$ |
|---|---|---|---|
| Roomdry | 0.34 | 0.52 | 0.14 |
| Roomdry 26 ppm $SO_2$ | 0.18 | 0.65 | 0.17 |
| Roomday 52 ppm $SO_2$ | 0.19 | 0.68 | 0.12 |
| Roomdry 106 ppm $SO_2$ | 0.20 | 0.65 | 0.14 |
| 80dry | 0.43 | 0.44 | 0.13 |
| 80dry 106 ppm $SO_2$ | 0.20 | 0.62 | 0.17 |

[a] The proportion of peak intensity was determined in each spectrum by dividing the specified peak intensity by the total peak intensity.

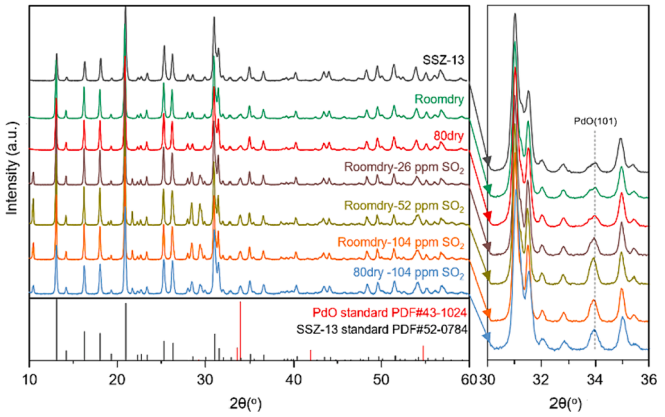


**Fig. 7.** XRD patterns of PNA samples before and after $SO_2$ poisoning. 'Roomdry' and '80dry' denote the Pd/SSZ-13 samples which were dried at room temperature or 80 °C after Pd impregnation.

follows:

$$k_j = A_j e^{\frac{-E_{A,j}}{(RT_s)}} \quad (2)$$

Here, for reaction j, $A_j$ represents the pre-exponential factor ($s^{-1}$), $E_{A,j}$ stands for the activation energy (J/mol), and $k_j$ refers to the rate constant j ($s^{-1}$). The Temkin isotherm was employed to linearly associate the activation energy with adsorption coverage [50]:

$$E_{des} = E^0_{des}(1 - \alpha\theta) \quad (3)$$

In this equation, $E^0_{des}$ symbolizes the desorption energy at zero coverage, α is the coverage dependence constant, and θ signifies the fractional coverage.

This reaction model comprises two elements: one describes the basic adsorption and release behaviors of $NO_x$, and the second part outlines the effects of $SO_2$ poisoning, which is the focus of the current work.

### 3.2.1. *Kinetic model for describing PNA performance before $SO_2$ poisoning*

Based on our previous kinetic model on PNA [17], we used a series of basic reactions to describe the $NO_x$ adsorption and release within the first two PNA test cycles. These were conducted in the presence of $NO_x$, $H_2O$, and $O_2$. Since no $SO_2$ was present in these initial cycles, no degradation of PNA was observed, as illustrated in Fig. S1 A, D. Consequently, no reactions involving $SO_2$ poisoning were included in the basic reaction model. The $NO_x$ adsorption and release profiles (Fig. 3), along with several prior studies [6,13,15,22,23], indicate that there are three initial Pd active sites: two ion-exchanged Pd sites (with and without a hydroxyl group, $Z^-Pd(II)Z^-$, $Z^-[Pd(II)OH]^+$), and one $Pd/PdO_x$ cluster on the external surface of zeolites. We categorized the reactions into three groups based on the initial Pd sites involved (Table 3). The first group, 'Reaction series Z', comprises reactions occurring at $Z^-Pd(II)Z^-$ sites, including the adsorption and release of NO and $NO_2$ species (Reactions Z1 and Z2). 'Reaction series ZH' includes reactions at $Z^-[Pd(II)OH]^+$ sites. This involves the adsorption and desorption of NO (Reaction ZH1), reduction of $Z^-[Pd(II)OH]^+$ to $Z^-Pd(I)$ (Reaction ZH2), adsorption and desorption of NO on $Z^-Pd(I)$ (Reaction ZH3), and re-

**Table 3**
Basic reaction model of passive $NO_x$ adsorption without $SO_2$ poisoning.

| Reactions | Reaction Step | Rate Expressions |
|---|---|---|
| Z1 | $Z^-Pd(II)Z^-$+NO ⇌ $Z^-Pd(II)Z^-$–NO | $r_{Z1} = k_{Z1f}\Psi_Z\theta_Z y_{NO} - k_{Z1b}\Psi_Z\theta_{Z\text{-}NO}$ |
| Z2 | $Z^-Pd(II)Z^-$+$NO_2$ ⇌ $Z^-Pd(II)Z^-NO_2$ | $r_{Z2} = k_{Z2f}\Psi_Z\theta_Z y_{NO2} - k_{Z2b}\Psi_Z\theta_{Z\text{-}NO2}$ |
| ZH1 | $Z^-[Pd(II)OH]^+$+NO ⇌ $Z^-[Pd(II)OH]^+$–NO | $r_{ZH1} = k_{ZH1f}\Psi_{ZH}\theta_{ZH1} y_{NO} - k_{ZH1b}\Psi_{ZH}\theta_{ZH1\text{-}NO}$ |
| ZH2 | $2Z^-[Pd(II)OH]^+$–NO ⇌ $Z^-Pd(I) + Z^-Pd(I)$–NO + $NO_2$ + $H_2O$ | $r_{ZH2} = k_{ZH2f}(\Psi_{ZH}\theta_{ZH1\text{-}NO})^2 - k_{ZH2b}\Psi_{ZH}\theta_{ZH2}\Psi_{ZH}\theta_{ZH2\text{-}NO}y_{NO2}y_{H2O}$ |
| ZH3 | $Z^-Pd(I)$ + NO ⇌ $Z^-Pd(I)$–NO | $r_{ZH3} = k_{ZH3f}\Psi_{ZH}\theta_{ZH2} y_{NO} - k_{ZH3b}\Psi_{ZH}\theta_{ZH2\text{-}NO}$ |
| ZH4 | $2Z^-Pd(I) + H_2O + 0.5O_2$ ⇌ $2Z^-[Pd(II)OH]^+$ | $r_{ZH4} = k_{ZH4f}(\Psi_{ZH}\theta_{ZH2})^2 y_{H2O} y_{O2}^{0.5} - k_{ZH4b}(\Psi_{ZH}\theta_{ZH1})^2$ |
| O1 | Pd(II)O + 2NO + $1.5O_2$ ⇌ $Pd(NO_3)_2$ | $r_{O1} = k_{O1f}\Psi_O\theta_{O1} y_{NO}^2 y_{O2}^{1.5} - k_{O1b}\Psi_O\theta_{O2}$ |
| O2 | $Pd(NO_3)_2$ + NO ⇌ Pd(II)O + $3NO_2$ | $r_{O2} = k_{O2f}\Psi_O\theta_{O2} y_{NO} - k_{O2b}\Psi_O\theta_{O1} y_{NO2}^3$ |

oxidation of $Z^-Pd(I)$ to $Z^-[Pd(II)OH]^+$ (Reaction ZH4). These reactions on $Z^-[Pd(II)OH]^+$ form a complete NO oxidation process, with the kinetic parameters aligning with thermodynamic reactions (Table 4). It is worth noting that the activation barrier for the reduction of $Z^-[Pd(II)OH]^+$ is significantly lower than for $Z^-Pd(II)Z^-$ reduction [24]. As a result, with increasing temperature, NO is unlikely to reduce $Z^-Pd(II)Z^-$ prior to desorption. The final reaction group, 'Reaction series O', contains the formation (Reaction O1) and decomposition (Reaction O2) of $Pd(NO_3)_2$. The kinetic parameters of these reactions also conform to thermodynamic constraints (Table 4).

Given the similar synthesis processes of Roomdry and 80dry samples (excluding the drying process), reactions at the Pd active sites in both samples should have identical kinetic parameters. However, the quantities of each Pd site are expected to vary between the two samples. The kinetic parameters of the basic reaction model are adjusted according to the NO and $NO_2$ profiles from the second cycle of both Roomdry and 80dry samples, as detailed in Table S1 and S2. Fig. 8 presents the NO and $NO_2$ profiles derived from this adjusted kinetic model, alongside the reference profiles from the experimental evaluation. There is a strong correlation between the simulated and experimental results. Notably, the ratio between $Z^-Pd(II)Z^-$ and $Z^-[Pd(II)OH]^+$ derived from the kinetic model matches the ratio calculated from in-situ DRIFT of CO adsorption, as outlined in Table 5. These findings suggest that the basic kinetic model and parameters effectively describe PNA performance prior to the introduction of $SO_2$ into the system.

### 3.2.2. *Kinetic model for $SO_2$ poisoning of $Z^-Pd(II)Z$*

Based on the evaluation and characterization results, the number of exposed $Z^-Pd(II)Z^-$ sites decreases after $SO_2$ poisoning, primarily due to $SO_2$ covering on the $Z^-Pd(II)Z^-$ site and deactivating its ability to store $NO_x$ species. Consequently, the adsorption of $SO_2$ on the $Z^-Pd(II)Z^-$ site is incorporated into the reaction model, as depicted in Reaction Z3 (Table 6). $SO_2$ anchoring on $Z^-Pd(II)Z^-$ forms an inactive $Z^-Pd(II)Z^-$-$SO_2$ site, which cannot contribute to $NO_x$ adsorption. There is no reverse reaction for Z3 because the NO desorption peak on $Z^-Pd(II)Z^-$ (at 290 °C) remains stable after terminating $SO_2$ exposure in cycles 8–12, as shown in Fig. 1C, F. This indicates that $Z^-Pd(II)Z^-$-SO2 is stable throughout the PNA multicycle test. The kinetic model results, incorporating Reaction Z3, are presented in Fig. 9. We selected the first and last cycles with $SO_2$ (cycles 3 and 7) and the first cycle after shutting off $SO_2$ (cycle 8) to represent the overall kinetic model. It should be noted that the kinetic modeling results for cycles 1 and 2 are unaffected by the addition of Reaction Z3, as no $SO_2$ is present in these cycles.

It can be seen in Fig. 9 that the NO release peak from $Z^-Pd(II)Z^-$ (at 290 °C) drastically decreased in the first cycle when adding $SO_2$ (cycle 3) in the kinetic modeling results, which also consists with our evaluation results. After shutting off $SO_2$ in cycle 8, all the NO desorption and conversion peaks as well as the $NO_2$ generation peak match well with the experimental results. From this result it also can be deduced that the Z-Pd(II)Z- sites were completely poisoned by $SO_2$, while Z-$[Pd(II)OH]^+$ can still maintain a similar NOx uptake as before $SO_2$ poisoning, because the peak at 460 °C did not change. On the contrary, in Cycle 3 and Cycle 7 we can see that the kinetic modeling result deviate from experimental results, mainly for the NO desorption at 460 °C and $NO_2$ formation at ~ 165 °C. The $NO_2$ generation peak at ~ 165 °C drastically decreased after adding $SO_2$, indicating that the reduction of Z-$[Pd(II)OH]^+$ to Z-Pd(I) is greatly suppressed. Given the derivation of these profiles, more reaction on Z-$[Pd(II)OH]^+$ should be added into the kinetic model.

**Table 4**
Thermodynamic restrictions of reaction model.

| Reactions | Overall reaction | Restriction on parameters |
|---|---|---|
| 2ZH1 + ZH2-ZH3 + ZH4 | $NO + 0.5O_2 \rightleftharpoons NO_2$ | $\Delta H_{NOox} = 2[E_{ZH1f}-E_{ZH1b}(1-\alpha_{ZH1b}\theta_{ZH1\text{-}NO})] + (E_{ZH2f}-E_{ZH2b}) - [E_{ZH3f}-E_{ZH5f}(1-\alpha_{ZH5f}\theta_{ZH2\text{-}NO})] + (E_{ZH4f}-E_{ZH4b})$<br>$\Delta S_{NOox} = 2Rln(A_{ZH1f}/A_{ZH1b}) + Rln(A_{ZH2f}/A_{ZH2b}) - Rln(A_{ZH3f}/A_{ZH5f}) + Rln(A_{ZH4f}/A_{ZH4b})$ |
| O2 + O3 | $3NO + 1.5O_2 \rightleftharpoons 3NO_2$ | $\Delta H_{NOox} = (E_{O2f}-E_{O2b}) + (E_{O3f}-E_{O3b})$<br>$\Delta S_{NOox} = Rln(A_{O2f}/A_{O2b}) + Rln(A_{O3f}/A_{O3b})$ |

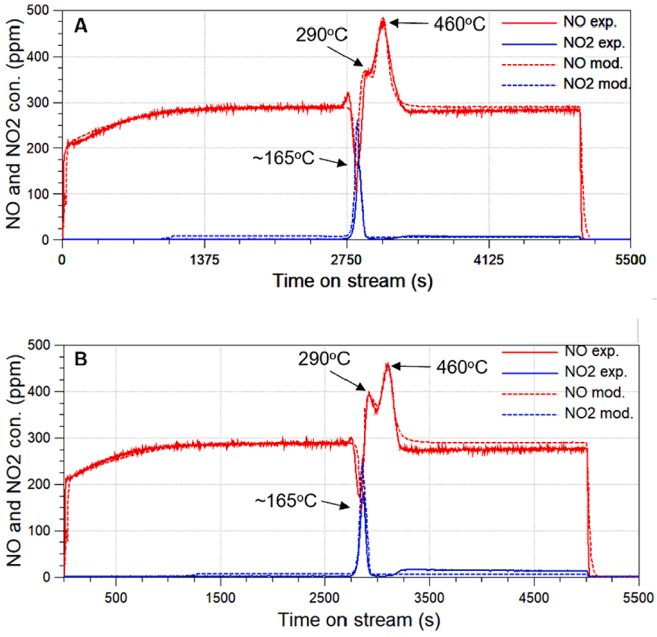


**Fig. 8.** Experimental and basic modeling results in Cycle 2 of Roomdry sample (A) and 80dry sample (B) in Cycle 2 (last cycle without $SO_2$). Reaction conditions: 290 ppm $NO_x$, $NO_2/NO_x$ = 1.8 %, 4.6 % $H_2O$, 6.9 % $O_2$ in Ar with the flow rate of 905 mL/min. 'Roomdry' and '80dry' denote the Pd/SSZ-13 samples which were dried at room temperature or 80 °C after Pd impregnation.

**Table 5**
Ratio between $Z^-Pd(II)Z^-$ and $Z^-[Pd(II)OH]^+$ in DRIFT and kinetic model.

| Samples | DRIFT | Model |
|---|---|---|
| Roomdry | 0.66 | 0.68 |
| 80dry | 0.98 | 0.95 |

**Table 6**
Reactions in kinetic model for describing $SO_2$ poisoning of $Z^-Pd(II)Z^-$.

| Reactions | Reaction Step | Rate Expressions |
|---|---|---|
| Z3 | $Z^-Pd(II)Z^- + SO2 \rightarrow Z^-Pd(II)Z^-SO_2$ | $r_{Z3} = k_{Z3f}\Psi_Z\theta_Z y_{SO2}$ |

### 3.2.3. *Kinetic model for describing $SO_2$ enhanced $NO_x$ adsorption on $Z^-[Pd(II)OH]^+$*

Evaluations depicted in Figs. 3 and 3, along with the kinetic model in Fig. 9, reveal that the NO desorption peak at 460 °C increases after adding $SO_2$. This clearly illustrates that $SO_2$ can enhance NO adsorption on $Z^-[Pd(II)OH]^+/Z^-Pd(I)$ sites. Moreover, Fig. 3 shows a gradual decrease in the NO release peak at 460 °C during the multicycle test with $SO_2$ (from cycle 3 to cycle 7), suggesting that $SO_2$ also slightly poisons the $Z^-[Pd(II)OH]^+/Z^-Pd(I)$ sites. However, after the termination of $SO_2$ (cycle 8), this peak maintains the same intensity as before $SO_2$ poisoning, indicating that the poisoned $Z^-[Pd(II)OH]^+/Z^-Pd(I)$ sites can be regenerated in the absence of $SO_2$. Furthermore, $SO_2$ is more likely to initially cover $Z^-[Pd(II)OH]^+$, thereby inhibiting the reduction of this site to $Z^-Pd(I)$. Based on these findings, we have introduced additional reactions (Table 7) showing that $Z^-[Pd(II)OH]^+$ can also be covered by $SO_2$ in a reversible reaction (reaction ZH5). The adsorbed $SO_2$ can further facilitate NO adsorption, as demonstrated in reactions

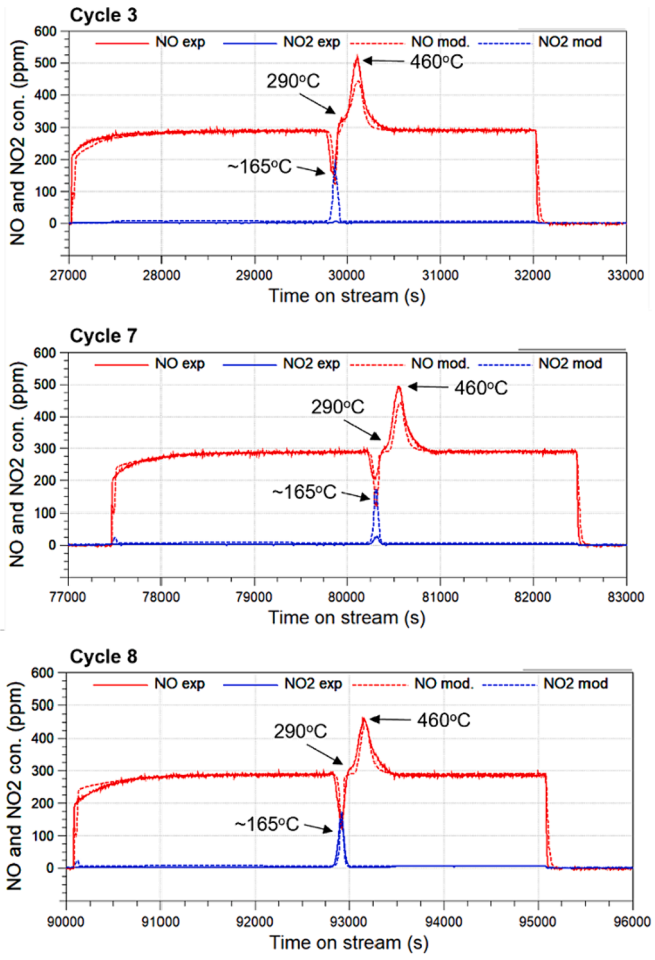


**Fig. 9.** Selected cycles of kinetic modeling results of 80dry Pd/SSSZ-13 sample with $SO_2$ poisoning reactions on $Z^-Pd(II)Z^-$ sites. Cycles: Cycle 3 (first cycle with $SO_2$), Cycle 7 (last cycle with $SO_2$) and Cycle 8 (first cycle shut $SO_2$). Reaction conditions: 290 ppm NOx, $NO_2/NO_x$ = 1.8 %, 104 ppm $SO_2$ (only in Cycle 3–7), 4.6 % $H_2O$, 6.9 % $O_2$ in Ar with the flow rate of 905 mL/min. '80dry' denote the Pd/SSZ-13 sample which was dried at 80 °C after Pd impregnation.

**Table 7**
Reactions in kinetic model for describing $SO_2$ enhanced $NO_x$ adsorption reactions on $Z^-[Pd(II)OH]^+$.

| Reactions | Reaction Step | Rate Expressions |
|---|---|---|
| ZH5 | $Z^-[Pd(II)OH]^+ + SO2 \rightleftharpoons Z^-[Pd(II)OH]^-SO_2$ | $r_{ZH5} = k_{ZH5f}\Psi_{ZH}\theta_{ZH1}y_{SO2} - k_{ZH5b}\Psi_{ZH}\theta_{ZH1\text{-}SO2}$ |
| ZH6 | $Z^-[Pd(II)OH]^-\text{-}SO_2 + NO \rightleftharpoons Z^-[Pd(II)OH]^-\text{-}SO_2\text{–}NO$ | $r_{ZH6} = k_{ZH6f}\Psi_{ZH}\theta_{ZH1\text{-}SO2}y_{NO} - k_{ZH6b}\Psi_{ZH}\theta_{ZH1\text{-}SO2\text{-}NO}$ |
| ZH7 | $Z^-[Pd(II)OH]^-$– NO + $SO_2 \rightleftharpoons Z^-[Pd(II)OH]^-$– NO – SO2 | $r_{ZH7} = k_{ZH7f}\Psi_{ZH}\theta_{ZH1\text{-}NO}y_{SO2} - k_{ZH7b}\Psi_{ZH}\theta_{ZH1\text{-}SO2\text{-}NO}$ |

ZH6 and ZH7.

The updated kinetic modeling results, accounting for the $SO_2$-enhanced $NO_x$ adsorption reactions on $Z^-[Pd(II)OH]^+$, are displayed in Fig. 10. With the reactions ZH5 to ZH7, the simulated NO and $NO_2$ profiles exhibit a better alignment with experimental results compared to the previous kinetic model. This is particularly evident at ~ 165 °C, where NO oxidation is significantly suppressed, leaving only small NO consumption and $NO_2$ generation peaks. However, there is still an issue remaining: at ~ 165 °C, the NO consumption peak area is actually larger than the $NO_2$ generation peaks. This suggests that another Pd site may be adsorbing NO at this temperature. It is important to note that $NO_x$ adsorption is a non-activated reaction [45,48,51], and therefore should occur at the beginning of the PNA process when $NO_x$ is introduced. Consequently, we can deduce that a new Pd site is generated at ~ 165 °C, which adsorbs $NO_x$ at a relatively high reaction rate. The stored NO on this newly generated Pd site is also released at 460 °C, subsequently increasing the peak intensity.

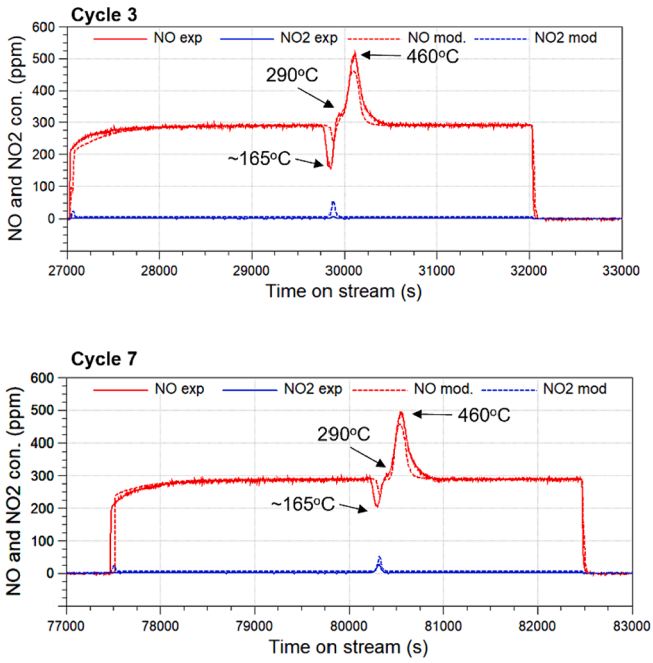


**Fig. 10.** Selected cycles of kinetic modeling results of 80dry with $SO_2$ enhanced $NO_x$ adsorption reactions on $Z^-[Pd(II)OH]^+$. Cycles: Cycle 3 (first cycle with $SO_2$), Cycle 7 (last cycle with $SO_2$). Reaction conditions: 290 ppm NOx, $NO_2/NO_x$ = 1.8 %, 104 ppm $SO_2$ (only in Cycle 3–7), 4.6 % $H_2O$, 6.9 % $O_2$ in Ar with the flow rate of 905 mL/min. '80dry' denote the Pd/SSZ-13 samples which was dried at 80 °C after Pd impregnation.

### 3.2.4. *Kinetic model for describing the formation of $PdSO_4$*

According to our kinetic model, which takes into account $SO_2$ poisoning of $Z^-Pd(II)Z^-$ and enhancement of $NO_x$ storage on $Z^-[Pd(II)OH]^+$, it becomes evident that new Pd sites are generated during the temperature rise in the TPD branch. These sites subsequently adsorb more NO and release it at higher temperatures. Numerous reports indicate that $PdO_x$ clusters can be transformed into $PdSO_4$ in the presence of gaseous $SO_2$, providing an additional adsorption site for $NO_x$ storage [52–54]. Consequently, we have incorporated two more reactions on $PdO_x$ sites to describe the formation of $PdSO_4$ (Reaction O3) and its adsorption of NO (Reaction O4), as detailed in Table 8. Note that Reaction O3 is reversible, given that $PdSO_4$ can decompose at higher temperatures [53]. The adjusted kinetic modeling results, alongside with the experimental results for the 80dry sample, are shown in Fig. 11 and Fig. S3. We have also validated the kinetic model based on the PNA performance for the Roomdry sample, as depicted in Fig. 12 and Fig. S6. Notably, while the initial Pd site amounts differ in the two PNA samples, all other kinetic parameters remain constant when simulating PNA performance across different samples. From the comparison results in Roomdry and 80dry, it is clear that the kinetic model can accurately describe PNA performance and $SO_2$ poisoning performance, regardless

**Table 8**
Reactions in kinetic model for describing the formation of $PdSO_4$.

| Reactions | Reaction Step | Rate Expressions |
|---|---|---|
| O3 | $PdO + SO_2 + 0.5O_2 \rightleftharpoons PdSO4$ | $r_{O3} = k_{O3f}\Psi_O\theta_{O1}y_{SO2}y_{O2}^{0.5} - k_{O3b}\Psi_O\theta_{O3}$ |
| O4 | $PdSO4 + NO \rightleftharpoons PdSO4\text{-}NO$ | $r_{O4} = k_{O4f}\Psi_O\theta_{O3}y_{NO} - k_{O4b}\Psi_O\theta_{O3\text{-}NO}$ |

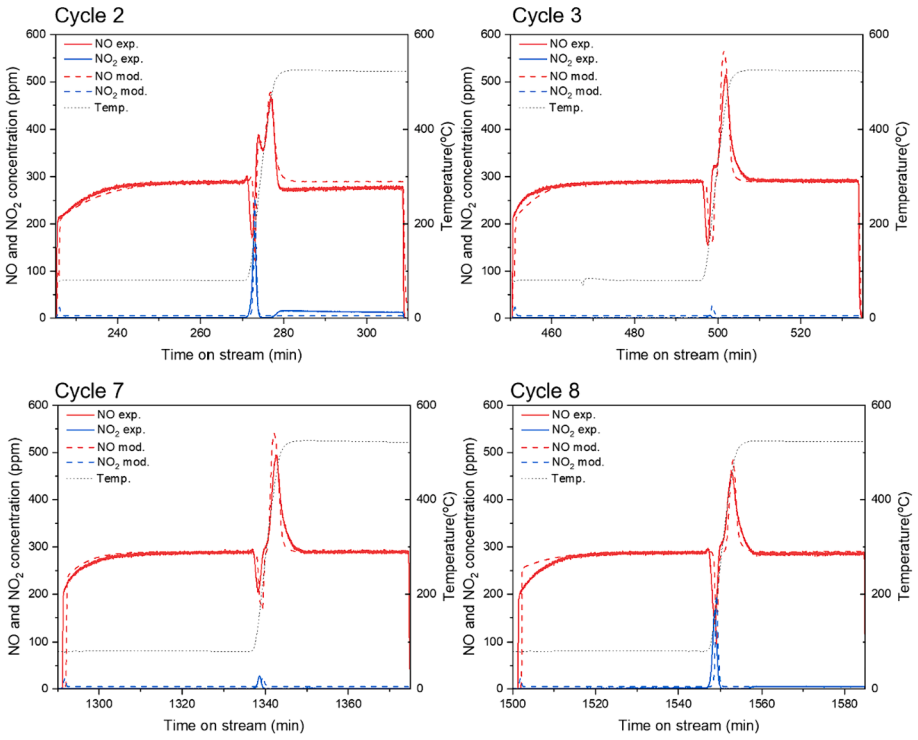


**Fig. 11.** Multi-cycle experimental and modeling results of 80dry sample in Cycle 2 (last cycle without $SO_2$), Cycle 3 (first cycle with $SO_2$), Cycle 7 (last cycle with $SO_2$) and Cycle 8 (first cycle shut $SO_2$). Reaction conditions: 290 ppm NOx, $NO_2/NO_x = 1.8$ %, 104 ppm $SO_2$ (only in Cycle 3–7), 4.6 % $H_2O$, 6.9 % $O_2$ in Ar with the flow rate of 905 mL/min. Adsorption temperature: 80 °C. Full cycle results are shown in Fig. S3. '80dry' denote the Pd/SSZ-13 samples which was dried at 80 °C after Pd impregnation.

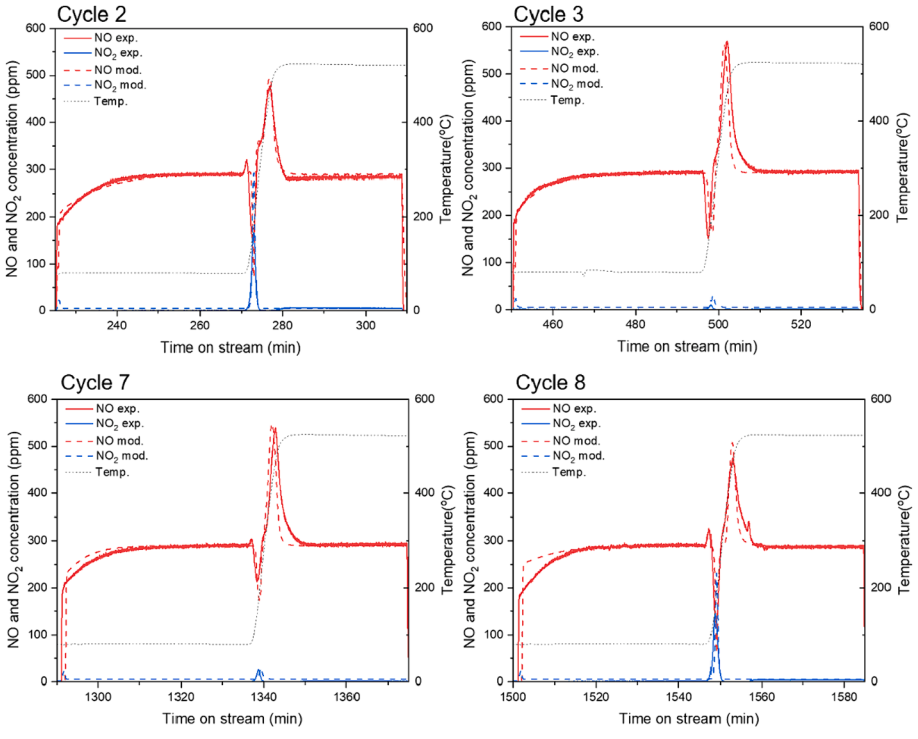


**Fig. 12.** Multi-cycle experimental and modeling results of Roomdry sample in Cycle 2 (last cycle without $SO_2$), Cycle 3 (first cycle with $SO_2$), Cycle 7 (last cycle with $SO_2$) and Cycle 8 (first cycle shut $SO_2$). Reaction conditions: 290 ppm NOx, $NO_2/NO_x = 1.8$ %, 104 ppm $SO_2$ (only in Cycle 3–7), 4.6 % $H_2O$, 6.9 % $O_2$ in Ar with the flow rate of 905 mL/min. Adsorption temperature: 80 °C. Full cycle results are shown in Fig. S6. 'Roomdry' denote the Pd/SSZ-13 samples which was dried at 80 °C after Pd impregnation.

of how the initial Pd sites change with different synthesis methods.

### 3.2.5. Verifying the kinetic model under different PNA operation conditions

Our developed model was further tested under a range of PNA operational conditions, applied to both Roomdry and 80dry samples, as depicted in Fig. S3 to S8. These conditions largely involved adjustments to the operational temperature in adsorption branch, ranging from 80 °C to 110 °C (Fig. S4) and up to 150 °C (Fig. S5), and reductions in the $SO_2$ concentration from 104 ppm to 52 ppm (Fig. S7) and down to 26 ppm (Fig. S8). The primary influence of the adsorption temperature variations can be seen in the NO oxidation peaks on PdO sites and the NO release peaks from $Z^-Pd(II)Z^-$. An increase in adsorption temperature results in that these peaks occuring earlier in time, while the $SO_2$ poisoning behavior stays relatively stable. Notably, the $NO_x$ desorption peak from $Z^-[Pd(II)OH]/Z^-Pd(I)$ at 460 °C does not change when the adsorption temperature is set to 150 °C. This finding supports our kinetic model, which describes that $SO_2$ mainly enhances $NO_x$ adsorption by generating new $PdSO_4$ sites, rather than aiding $NO_x$ adsorption on $Z^-[Pd(II)OH]/Z^-Pd(I)$. The concentration of $SO_2$ predominantly influences the desorption of $NO_x$ from $PdSO_4$ at 460 °C. With an increase in $SO_2$ concentration, more $PdSO_4$ forms, leading to an increase in $NO_x$ adsorption and its subsequent release at 460 °C. The NO adsorption on $Z^-Pd(II)Z^-$ remains unaffected by changes in $SO_2$ concentration due to the relatively high poisoning rate of $Z^-Pd(II)Z^-$.

In order to delve deeper into the contribution of various reactions and kinetic parameters to the kinetic modeling of sulfur poisoning in PNA, we calculated the normalized sensitivity coefficients of the kinetic parameters, based on model validation. It is important to note that normalized sensitivity is a dimensionless constant. A higher value of normalized sensitivity suggests that the kinetic model is more susceptible to the corresponding kinetic parameter, which in turn is more accurate in predicting experimental behavior. To calculate the normalized sensitivity, we incremented only one kinetic parameter by 1 % at each time in the simulation to obtain the deviated simulation result. This process incorporated 666,000 data points from the NO profile and another 666,000 data points from the $NO_2$ profile under various operation conditions, as demonstrated from Fig. S3 to Fig. S8. The normalized sensitivity coefficients were then determined using the following equation:

$$S = \beta_0 \frac{\sum \left(\frac{\Delta y^{sim}}{y_0^{sim}}\right)^2}{\Delta\beta} \quad (4)$$

where $\beta_0$ represents the optimized parameter, $\Delta\beta$ is the deviated value of the changed parameter from the optimized parameter. $y_0^{sim}$ is the NO/$NO_2$ concentration at one time point from the optimized value. $\Delta y^{sim}$ is the deviation in NO/$NO_2$ concentration between the optimized result and the result with the changed parameter.

We arranged the kinetic parameters in descending order, from the highest to the lowest normalized sensitivity, as depicted in Fig. 13. The parameters with the greatest influence on the NO profiles are Af-O4, Af/Ab-ZH3, and Af/Ab-ZH5. Reaction O4, which describes the NO adsorption and desorption on $PdSO_4$ (Table 8), influences both the NO consumption peak at approximately 165 °C and the NO desorption peak at 460 °C following the addition of $SO_2$. Due to its effect on these two peaks in the NO profiles, Af-O4 emerges as the most sensitive parameter for the kinetic model. Reactions ZH3 (Table 3) and ZH5 (Table 7) predominantly describe the NO adsorption on Z-Pd(I), which is reduced from $Z^-[Pd(II)OH]^+$, and $SO_2$ adsorption on $Z^-[Pd(II)OH]^+$. These reactions are sensitive to the kinetic model as they contribute to the dominant NO desorption peak at 460 °C, with or without $SO_2$. Although Af-Z3, Af-Z2, Af-O1, and Af-O2 display the least sensitivity towards the kinetic modeling results, they remain crucial to the overall reaction model. Af-Z3 describes the $SO_2$ poisoning on $Z^-Pd(II)Z^-$ sites (Table 6). The rate of this reaction needs to be high enough to ensure that the $Z^-Pd(II)Z^-$ are poisoned in the first cycle with $SO_2$, thereby reducing the sensitivity of Af-Z3. Af-Z2 contributes to the $NO_2$ profile, so its sensitivity on the NO profile can be neglected. The relatively lesser sensitivity of $O_1$ and O2 is due to the slow formation of $Pd(NO_3)_2$ compared to other reactions because the $Pd(NO_3)_2$ only partially formed in the first two cycles without $SO_2$ adding. However, these reactions must be retained because we have observed the formation of $Pd(NO_3)_2$ in our previous work [17].

The sensitivity of parameters on $NO_2$ profiles is lower than on NO profiles due to the significantly lower $NO_2$ concentration in the PNA process. The parameters that most significantly influence the $NO_2$ profiles are Af-O3 and Af-Z1. Reaction O3 strongly suppresses the formation of $Pd(NO_3)_2$ at ~ 165 °C, leading to its subsequent decomposition and $NO_2$ release. Given the competitive adsorption of NO and $NO_2$ on Z-Pd(II)Z-, the adsorption rate of NO significantly influences the adsorption of $NO_2$, which explains why reaction Z1 also greatly influences the $NO_2$ profile. The less sensitive parameters based on the $NO_2$ profiles are more sensitive towards simulated NO profiles, indicating that those corresponding reactions are also critical to this kinetic model.

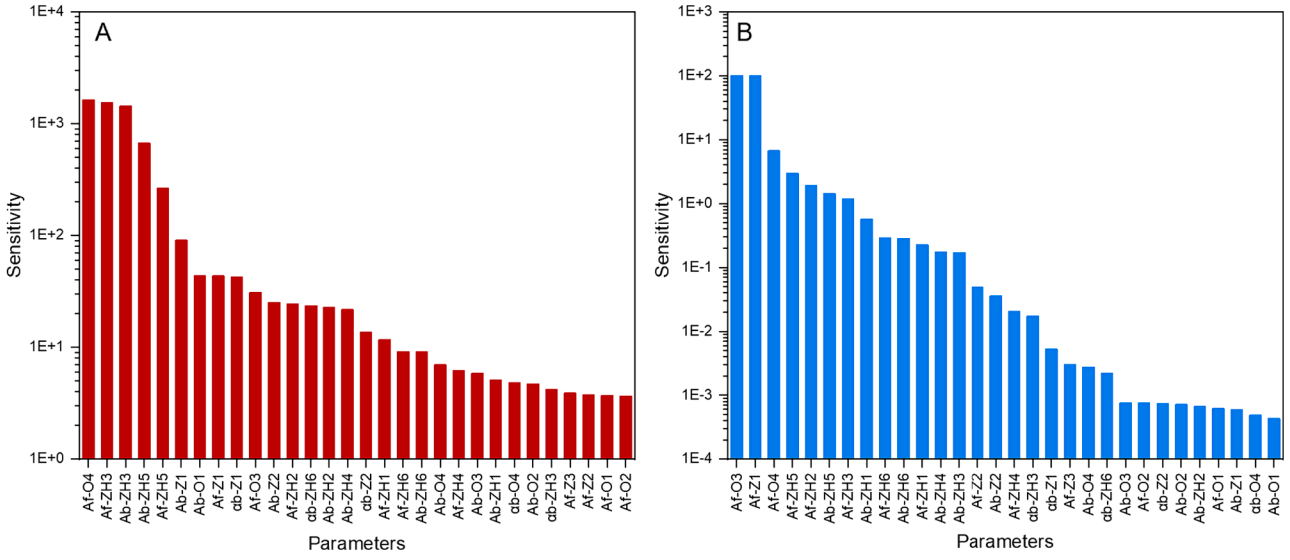


**Fig. 13.** Normalized sensitivity co-efficient of kinetic parameters based on NO profiles (A) and $NO_2$ profiles (B).

## 4. Conclusions

In this study, we explored the $SO_2$ poisoning mechanism through a combined experimental and kinetic modeling approach, and also developed an innovative PNA sample exhibiting strong resistance to $SO_2$ poisoning. Pd/SSZ-13 samples were synthesized using the impregnation method but under varying drying conditions—room temperature drying and 80 °C drying—to create different surface distributions of Pd active sites. Our multicycle PNA tests with $SO_2$ poisoning revealed that the Roomdry sample experienced a 10 % degradation, while the 80dry sample experienced a considerably greater degradation of 26 %.

Upon conducting in-situ DRIFT of CO adsorption, XRD, and TEM for the degreened and poisoned samples, we discovered that the ion-exchanged Pd sites with a hydroxyl group ($Z^-[Pd(II)OH]^+$) demonstrated strong resistance to $SO_2$ poisoning, whereas $Z^-Pd(II)Z^-$ was notably vulnerable to $SO_2$ poisoning. By reducing the drying temperature after the Pd/SSZ-13 loading process, we were able to generate more ion-exchanged Pd sites with a hydroxyl group, which explains the high $SO_2$ tolerance of the Roomdry sample. Moreover, we found that $SO_2$ also aids in $NO_x$ storage on both $Z^-[Pd(II)OH]^+$ and $PdO_x$ sites, resulting in improved PNA performance.

Based on these experimental findings, we developed a kinetic model that can describe both the $SO_2$ poisoning behavior of PNA and the role of $SO_2$ in assisting $NO_x$ storage. The kinetic model incorporates three initial Pd sites, $Z^-Pd(II)Z^-$, $Z^-[Pd(II)OH]^+$, and PdO, with 14 reactions. The model accounts for the $SO_2$ poisoning of $Z^-Pd(II)Z^-$ and $Z^-[Pd(II)OH]^+$, as well as the enhancement of $NO_x$ storage on $Z^-[Pd(II)OH]^+$ and PdO due to $SO_2$. After being verified under different reaction conditions, this model has proven its robustness in simulating the PNA behavior and the influence of $SO_2$ in multicycle PNA tests, including varying $SO_2$ concentrations (26 ~ 104 ppm), different operation temperatures in adsorption branch (80 ~ 150 °C), and even different PNA samples. We also calculated the normalized sensitivity of different reaction parameters by varying the kinetic parameters and comparing them with the optimized results. This analysis demonstrated that all the reactions in this kinetic model are crucial for accurately describing PNA behavior.

## CRediT authorship contribution statement

**Dawei Yao:** Writing – original draft, Methodology, Investigation, Formal analysis, Data curation, Conceptualization. **Phuoc Hoang Ho:** Writing – review & editing, Formal analysis, Data curation. **Johann C. Wurzenberger:** . **Thomas Glatz:** Writing – review & editing, Supervision, Software. **Wei Di:** Data curation, Formal analysis. **Rojin Feizie Ilmasani:** . **Derek Creaser:** Writing – review & editing, Supervision, Methodology, Conceptualization. **Louise Olsson:** Writing – review & editing, Supervision, Methodology, Funding acquisition, Conceptualization.

## Declaration of competing interest

The authors declare the following financial interests/personal relationships which may be considered as potential competing interests: Johann C. Wurzenberger and Thomas Glatz reports a relationship with AVL List GmbH that includes: employment. Louise Olsson is one of the Editors for Chemical Engineering Journal.

## Data availability

Data will be made available on request.

## Acknowledgements

This research was carried out at the Division of Chemical Engineering and the Competence Center for Catalysis at Chalmers University of Technology, located in Gothenburg, Sweden, and was done in partnership with AVL List GmbH, based in Graz, Austria. The funding for this project was provided by the European Union's Horizon 2020 research and innovation programme, under the grant agreement number 874972.

## Appendix A. Supplementary data

Supplementary data to this article can be found online at https://doi.org/10.1016/j.cej.2024.150406.

## References

[1] C. Weber, I. Sundvor, E. Figenbaum, Comparison of regulated emission factors of euro 6 LDV in nordic temperatures and cold start conditions: diesel- and gasoline direct-injection, Atmos. Enviro. 206 (2019) 208–217, https://doi.org/10.1016/j.atmosenv.2019.02.031.
[2] J. Gao, G. Tian, A. Sorniotti, A.E. Karci, R. Di Palo, Review of thermal management of catalytic converters to decrease engine emissions during cold start and warm up, Appl. Therm. Eng. 147 (2019) 177–187, https://doi.org/10.1016/j.applthermaleng.2018.10.037.
[3] R. O'Driscoll, M.E.J. Stettler, N. Molden, T. Oxley, H.M. ApSimon, Real world CO2 and NOx emissions from 149 euro 5 and 6 diesel, gasoline and hybrid passenger cars, Sci. Total Environ. 621 (2018) 282–290, https://doi.org/10.1016/j.scitotenv.2017.11.271.
[4] A. Wang, L. Olsson, The impact of automotive catalysis on the United Nations sustainable development goals, Nat. Catal. 2 (7) (2019) 566–570, https://doi.org/10.1038/s41929-019-0318-3.
[5] Y. Gu, W.S. Epling, Passive NOx adsorber: an overview of catalyst performance and reaction chemistry, Appl. Catal. A-Gen. 570 (2019) 1–14, https://doi.org/10.1016/j.apcata.2018.10.036.
[6] A. Wang, K. Xie, A. Kumar, K. Kamasamudram, L. Olsson, Layered PD/SSZ-13 with CU/SSZ-13 as PNA − SCR dual-layer monolith catalyst for NOx abatement, Catal. Today (2020) 356–366, https://doi.org/10.1016/j.cattod.2020.01.035.
[7] H.-Y. Chen, J.E. Collier, D. Liu, L. Mantarosie, D. Durán-Martín, V. Novák, R. R. Rajaram, D. Thompsett, Low temperature NO storage of zeolite supported pd for low temperature diesel engine emission control, Catal. Lett. 146 (9) (2016) 1706–1711, https://doi.org/10.1007/s10562-016-1794-6.
[8] J. Lee, J.R. Theis, E.A. Kyriakidou, Vehicle emissions trapping materials: successes, challenges, and the path forward, Appl. Catal. B-Environ. 243 (2019) 397–414, https://doi.org/10.1016/j.apcatb.2018.10.069.
[9] Y. Ryou, J. Lee, Y. Kim, S. Hwang, H. Lee, C.H. Kim, D.H. Kim, Effect of reduction treatments (H2 vs. CO) on the NO adsorption ability and the physicochemical properties of PD/SSZ-13 passive NOx adsorber for cold start application, Appl. Catal. A-Gen. 569 (2019) 28–34, https://doi.org/10.1016/j.apcata.2018.10.016.
[10] Y. Gu, R.P. Zelinsky, Y.-R. Chen, W.S. Epling, Investigation of an irreversible NOx storage degradation mode on a PD/BEA passive NOx adsorber, Appl. Catal. B-Environ. 258 (2019) 118032, https://doi.org/10.1016/j.apcatb.2019.118032.
[11] D. Li, Y. Meng, D. Hao, Q. Ding, L. Pang, G. Yang, Y. Guo, J. Yu, T. Li, Deactivation of PD/SSZ-13 passive NOx adsorber from the perspectives of phosphorus poisoning and hydrothermal aging, Chem. Eng. J. 446 (2022), https://doi.org/10.1016/j.cej.2022.136779.
[12] R.F. Ilmasani, D. Yao, P.H. Ho, D. Bernin, D. Creaser, L. Olsson, Deactivation of phosphorus-poisoned PD/SSZ-13 for the passive adsorption of NOx, J. Environ. Chem. Eng. 10 (3) (2022) 107608, https://doi.org/10.1016/j.jece.2022.107608.
[13] D. Chen, H. Lei, W. Xiong, Y. Li, X. Ji, J.-Y. Yang, B. Peng, M. Fu, P. Chen, D. Ye, Unravelling phosphorus-induced deactivation of pd-SSZ-13 for passive NOx adsorption and CO oxidation, ACS Catal. (2021) 13891–13901, https://doi.org/10.1021/acscatal.1c03214.
[14] R.R. Rajaram, H.-Y. Chen, D. Liu, Passive NOx Adsorber US10005075B2 (2014).
[15] D. Yao, P.H. Ho, R.F. Ilmasani, J.C. Wurzenberger, T. Glatz, D. Creaser, L. Olsson, Enhanced CO resistance of PD/SSZ-13 for passive NOx adsorption, Chem. Eng. J. 460 (2023), https://doi.org/10.1016/j.cej.2023.141681.
[16] D. Yao, R.F. Ilmasani, J.C. Wurzenberger, T. Glatz, J. Han, P.H. Ho, D. Creaser, L. Olsson, Insight into CO induced degradation mode of PD/SSZ-13 in NOx adsorption and release: experiment and modeling, Chem. Eng. J. 439 (2022) 135714, https://doi.org/10.1016/j.cej.2022.135714.
[17] D. Yao, R.F. Ilmasani, J.C. Wurzenberger, T. Glatz, J. Han, A. Wang, D. Creaser, L. Olsson, Kinetic modeling of CO assisted passive NOx adsorption on PD/SSZ-13, Chem. Eng. J. 428 (2022) 132459, https://doi.org/10.1016/j.cej.2021.132459.
[18] P.H. Ho, D. Yao, D. Creaser, L. Olsson, Advantages of high-siliceous zeolites in the reactivity and stability of diesel oxidation catalysts, ACS Eng. Au (2022), https://doi.org/10.1021/acsengineeringau.1c00035.
[19] S. Ghosh, L. Olsson, D. Creaser, Methanol mediated direct CO2 hydrogenation to hydrocarbons: experimental and kinetic modeling study, Chem. Eng. J. 435 (2022), https://doi.org/10.1016/j.cej.2022.135090.
[20] V. Mesilov, S. Dahlin, S.L. Bergman, S. Xi, J. Han, L. Olsson, L.J. Pettersson, S. L. Bernasek, Regeneration of sulfur-poisoned cu-SSZ-13 catalysts: copper speciation and catalytic performance evaluation, Appl. Catal. B-Environ. 299 (2021), https://doi.org/10.1016/j.apcatb.2021.120626.
[21] S. Yasumura, H. Ide, T. Ueda, Y. Jing, C. Liu, K. Kon, T. Toyao, Z. Maeno, K.-I. Shimizu, Transformation of bulk pd to pd cations in small-pore CHA zeolites

facilitated by NO, JACS Au 1 (2) (2021) 201–211, https://doi.org/10.1021/jacsau.0c00112.
[22] M. Ambast, A. Gupta, B.M.M. Rahman, L.C. Grabow, M.P. Harold, NOx adsorption with CO and $C_2H_4$ on PD/SSZ-13: experiments and modeling, Appl. Catal. B-Environ. 286 (2021) 119871, https://doi.org/10.1016/j.apcatb.2020.119871.
[23] M. Ambast, K. Karinshak, B.M.M. Rahman, L.C. Grabow, M.P. Harold, Passive NOx adsorption on Pd/H-ZSM-5: experiments and modeling, Appl. Catal. B-Environ. 269 (2020) 118802, https://doi.org/10.1016/j.apcatb.2020.118802.
[24] D. Mei, F. Gao, J. Szanyi, Y. Wang, Mechanistic insight into the passive NOx adsorption in the highly dispersed PD/HBEA zeolite, Appl. Catal. A-Gen. 569 (2019) 181–189, https://doi.org/10.1016/j.apcata.2018.10.037.
[25] A. Wang, K. Lindgren, M. Di, D. Bernin, P.-A. Carlsson, M. Thuvander, L. Olsson, Insight into hydrothermal aging effect on pd sites over PD/LTA and PD/SSZ-13 as PNA and CO oxidation monolith catalysts, Appl. Catal. B-Environ. 278 (2020) 119315, https://doi.org/10.1016/j.apcatb.2020.119315.
[26] Y. Zheng, L. Kovarik, M.H. Engelhard, Y. Wang, Y. Wang, F. Gao, J. Szanyi, Low-temperature Pd/zeolite passive NOx adsorbers: structure, performance, and adsorption chemistry, J. Phys. Chem. C 121 (29) (2017) 15793–15803, https://doi.org/10.1021/acs.jpcc.7b04312.
[27] K. Honkala, P. Pirila, K. Laasonen, CO and NO adsorption and co-adsorption on the Pd(111) surface, Surf. Sci. 489 (2001), https://doi.org/10.1016/S0039-6028(01)01135-9.
[28] K. Khivantsev, N.R. Jaegers, L. Kovarik, J.C. Hanson, F.F. Tao, Y. Tang, X. Zhang, I. Z. Koleva, H.A. Aleksandrov, G.N. Vayssilov, Y. Wang, F. Gao, J. Szanyi, Achieving atomic dispersion of highly loaded transition metals in small-pore zeolite SSZ-13: high-capacity and high-efficiency low-temperature CO and passive NOx adsorbers, Angew. Chem. Int. Ed. 57 (51) (2018) 16672–16677, https://doi.org/10.1002/anie.201809343.
[29] K. Khivantsev, N.R. Jaegers, I.Z. Koleva, H.A. Aleksandrov, L. Kovarik, M. Engelhard, F. Gao, Y. Wang, G.N. Vayssilov, J. Szanyi, Stabilization of super electrophilic Pd+2 cations in small-pore SSZ-13 zeolite, J. Phys. Chem. C 124 (1) (2020) 309–321, https://doi.org/10.1021/acs.jpcc.9b06760.
[30] H. Zhao, X. Chen, A. Bhat, Y. Li, J.W. Schwank, Insight into hydrothermal aging effect on deactivation of PD/SSZ-13 as low-temperature NO adsorption catalyst: effect of dealumination and pd mobility, Appl. Catal. B-Environ. 286 (2021), https://doi.org/10.1016/j.apcatb.2020.119874.
[31] L. Castoldi, R. Matarrese, S. Morandi, P. Ticali, L. Lietti, Low-temperature PD/FER NOx adsorbers: operando FT-IR spectroscopy and performance analysis, Catal. Today 360 (2021) 317–325, https://doi.org/10.1016/j.cattod.2020.02.019.
[32] A.W. Aylor, L.J. Lobree, J.A. Reimer, A.T. Bell, Investigations of the dispersion of pd in H-ZSM-5, J. Catal. 172 (1997) 453–462.
[33] K. Khivantsev, X. Wei, L. Kovarik, N.R. Jaegers, E.D. Walter, P. Tran, Y. Wang, J. Szanyi, Palladium/Ferrierite versus PALLADIUM/SSZ-13 passive NOx adsorbers: adsorbate-controlled location of atomically dispersed PALLADIUM(II) in ferrierite determines high activity and stability, Angew. Chem. Int. Ed. Engl. 61 (3) (2022) e202107554.
[34] J. Luo, F. Gao, K. Kamasamudram, N. Currier, C.H.F. Peden, A. Yezerets, New insights into CU/SSZ-13 SCR catalyst acidity. part I: nature of acidic sites probed by NH3 titration, Journal of Catalysis 348 (2017) 291–299, https://doi.org/10.1016/j.jcat.2017.02.025.
[35] R. Villamaina, S. Liu, I. Nova, E. Tronconi, M.P. Ruggeri, J. Collier, A. York, D. Thompsett, Speciation of cu cations in cu-CHA catalysts for NH3-SCR: effects of SiO2/AlO3 ratio and cu-loading investigated by transient response methods, ACS Catal. 9 (10) (2019) 8916–8927, https://doi.org/10.1021/acscatal.9b02578.
[36] M.S. Wilburn, W.S. Epling, Formation and decomposition of sulfite and sulfate species on Pt/Pd catalysts: an SO2 oxidation and sulfur exposure study, ACS Catal. 9 (1) (2018) 640–648, https://doi.org/10.1021/acscatal.8b03529.
[37] C.C. Chang, Infrared studies of SO2 on γ-alumina, J. Catal. 53 (3) (1978) 374–385, https://doi.org/10.1016/0021-9517(78)90109-4.
[38] M.S. Wilburn, W.S. Epling, SO 2 adsorption and desorption characteristics of pd and pt catalysts: precious metal crystallite size dependence, Appl. Catal. A-Gen. 534 (2017) 85–93, https://doi.org/10.1016/j.apcata.2017.01.015.
[39] D.L. Mowery, R.L. McCormick, Deactivation of alumina supported and unsupported PdO methane oxidation catalyst: the effect of water on sulfate poisoning, Appl. Catal. B-Environ. 34 (4) (2001) 287–297, https://doi.org/10.1016/S0926-3373(01)00222-3.
[40] A. Datta, R.G. Cavell, R.W. Tower, Z.M. George, Claus catalysis. 1. adsorption of sulfur dioxide on the alumina catalyst studied by FTIR and EPR spectroscopy, J. Phys. Chem. 89 (1985) 443–449.
[41] S. Shwan, L. Olsson, M. Skoglundh, J. Jansson, Kinetic modeling of fe-BEA as NH3-SCR catalyst—effect of phosphorous, AIChE J 61 (1) (2015) 215–223, https://doi.org/10.1002/aic.14638.
[42] X. Auvray, W. Partridge, J.-S. Choi, J. Pihl, F. Coehlo, A. Yezerets, K. Kamasamudram, N. Currier, L. Olsson, Kinetic modeling of $NH_3$-SCR over a supported cu zeolite catalyst using axial species distribution measurements, Appl. Catal. B-Environ. 163 (2015) 393–403, https://doi.org/10.1016/j.apcatb.2014.08.003.
[43] L. Olsson, M. Fredriksson, R.J. Blint, Kinetic modeling of sulfur poisoning and regeneration of lean NOx traps, Appl. Catal. B-Environ. 100 (1–2) (2010) 31–41, https://doi.org/10.1016/j.apcatb.2010.07.004.
[44] L. Olsson, H. Sjövall, R.J. Blint, A kinetic model for ammonia selective catalytic reduction over cu-ZSM-5, Appl. Catal. B-Environ. 81 (3–4) (2008) 203–217, https://doi.org/10.1016/j.apcatb.2007.12.011.
[45] L. Olsson, K. Wijayanti, K. Leistner, A. Kumar, S.Y. Joshi, K. Kamasamudram, N. W. Currier, A. Yezerets, A multi-site kinetic model for NH3-SCR over CU/SSZ-13, Appl. Catal. B-Environ. 174 (2015) 212–224, https://doi.org/10.1016/j.apcatb.2015.02.037.
[46] A.L. GmbH, AVL BOOST Aftertreatment Manual, (2020).
[47] D. Chatterjee, T. Burkhardt, B. Bandl-Konrad, T. Braun, E. Tronconi, I. Nova, C. Ciardelli, Numerical simulation of ammonia SCR-catalytic converters: model development and application, SAE Trans. 114 (2005) 437–448.
[48] L. Olsson, K. Wijayanti, K. Leistner, A. Kumar, S.Y. Joshi, K. Kamasamudram, N. W. Currier, A. Yezerets, A kinetic model for sulfur poisoning and regeneration of CU/SSZ-13 used for $NH_3$-SCR, Appl. Catal. B-Environ. 183 (2016) 394–406, https://doi.org/10.1016/j.apcatb.2015.11.001.
[49] N. Wilken, K. Kamasamudram, N.W. Currier, J. Li, A. Yezerets, L. Olsson, Heat of adsorption for NH3, NO2 and NO on cu-Beta zeolite using microcalorimeter for NH3 SCR applications, Catal. Today 151 (3) (2010) 237–243, https://doi.org/10.1016/j.cattod.2010.02.002.
[50] L. Olsson, H. Sjövall, R.J. Blint, Detailed kinetic modeling of NOx adsorption and NO oxidation over cu-ZSM-5, Appl. Catal. B-Environ. 87 (3) (2009) 200–210, https://doi.org/10.1016/j.apcatb.2008.09.007.
[51] L. Olsson, H. Sjövall, R.J. Blint, Detailed kinetic modeling of NOx adsorption and NO oxidation over cu-ZSM-5, Appl. Catal. B-Environ. 87 (3–4) (2009) 200–210, https://doi.org/10.1016/j.apcatb.2008.09.007.
[52] Z. Zhang, L. Sun, X. Hu, Y. Zhang, H. Tian, X. Yang, Anti-sintering PD@SILICALITE-1 for methane combustion: effects of the moisture and SO2, Appl. Surf. Sci. 494 (2019) 1044–1054, https://doi.org/10.1016/j.apsusc.2019.07.252.
[53] G. Li, K. Shen, P. Wu, Y. Zhang, Y. Hu, R. Xiao, B. Wang, S. Zhang, SO(2) poisoning mechanism of the multi-active center catalyst for chlorobenzene and NO(X) synergistic degradation at dry and humid environments, Environ. Sci. Tech. 55 (19) (2021) 13186–13197, https://doi.org/10.1021/acs.est.1c03617.
[54] H.N. Sharma, V. Sharma, T. Hamzehlouyan, W. Epling, A.B. Mhadeshwar, R. Ramprasad, SOx oxidation kinetics on Pt(111) and Pd(111): first-principles computations meet microkinetic modeling, J. Phys. Chem. C 118 (13) (2014) 6934–6940, https://doi.org/10.1021/jp501538v.